

AUTHOR QUERIES

AUTHOR PLEASE ANSWER ALL QUERIES

PLEASE NOTE: We cannot accept new source files as corrections for your article. If possible, please annotate the PDF proof we have sent you with your corrections and upload it via the Author Gateway. Alternatively, you may send us your corrections in list format. You may also upload revised graphics via the Author Gateway.

Carefully check the page proofs (and coordinate with all authors); additional changes or updates **WILL NOT** be accepted after the article is published online/print in its final form. Please check author names and affiliations, funding, as well as the overall article for any errors prior to sending in your author proof corrections.

AQ:1 = Please confirm or add details for any funding or financial support for the research of this article.

AQ:2 = Please provide the expansion of the acronym EPSRC for your funding agency. Providing the correct acknowledgment will ensure proper credit to the funder.

AQ:3 = Please confirm whether the edits made in the past/current affiliation of all the authors are correct.

AQ:4 = Please provide the full current affiliation details (department name, name of university/institution, city, state/country, zip/postal code) for the author Alex Grievson.

AQ:5 = Please provide the appropriate section number for the phrase “following sections.”

AQ:6 = Please provide the month for Ref. [7].

Point-Spread Analysis of γ -Ray/Depth Spectra for Borehole Monitoring Applications

Soraia C. Elísio, Aliyu Bala, Manuel Bandala, James Graham, Alex Grievson,
and Malcolm J. Joyce[✉], *Member, IEEE*

Abstract—An approach to the analysis of γ -ray spectra that might arise as depth profiles from the characterization of radioactivity in boreholes is described. A borehole logging probe, “ABACUS,” has been designed and constructed, which comprises a cerium bromide detector and a built-in multichannel analyzer (MCA). This has been tested in a bespoke, laboratory-based testbed built to replicate the borehole environment. An established, semiempirical model has been applied to data arising from the cerium bromide scintillation detector to extract the number of counts under the full-energy peak from each of the resulting γ -ray spectra (in this case the 662 keV line from ^{137}Cs) associated with each depth position, which also enables this information to be isolated from other contributions such as background and the Compton continuum. A complementary approach has been adopted to process the asymmetric and non-Gaussian trend that concerns the full-energy peak count as a function of depth in the borehole testbed for a given depth profile when the testbed is subject to the activity provided by a sealed, ^{137}Cs source. This comprises a modified, Moffat point-spread function (PSF). The Moffat function is a continuous probability distribution based on the Lorentzian distribution. Its particular importance is due to its ability to reconstruct PSFs that comprise wings that cannot be reproduced accurately by either a Gaussian or Lorentzian function. This application of the Moffat formalism to radioactive contamination assessment profiles enables an effective and accurate assessment to be made of the position of localized radioactivity in the testbed wall.

Index Terms— γ -ray detection, curve fitting, Gaussian distribution, nuclear measurements, radioactive pollution.

NOMENCLATURE

Glossary

- A* Amplitude of Gaussian function applied to photopeak.
- B* Amplitude of step function expressed as a fraction of *A*.
- b* Offset representing the residual background count.

- β Parameter governing the shape of a depth profile.
- C* Tail function amplitude expressed as a fraction of *A*.
- df* Number of degrees of freedom.
- f* Spectrum fitting function.
- G* Gaussian function.
- g* Moffat point-spread function (PSF).
- γ Skew parameter of the peak of a depth profile.
- I* Amplitude of a Moffat PSF.
- μ Centroid of the Gaussian function applied to photopeak.
- m* Slope of the exponential in the tail function, *T*.
- N* Number of counts in photopeak.
- n* Constant in Gaussian integral ensuring 3σ coverage.
- p* Peak depth position as per centroid components below.
- p_x Centroid in *x* of an image or depth profile.
- p_y Centroid in *y* of an image or depth profile.
- S* Step discontinuity function in photon spectrum.
- s* Sigmoid-type function describing *x*-axis asymmetry.
- σ Standard deviation of the Gaussian applied to photopeak.
- T* Tail function applied to photon spectrum.
- w_x Parameter governing the width of a depth profile in *x*.
- w_y Parameter governing the width of a depth profile in *y*.
- x_0 Central *x* coordinate of an elliptic profile.
- y_0 Central *y* coordinate of an elliptic profile.
- x* Abscissa denoting photon energy or depth.
- y* Parameter orthogonal to depth in Moffat PSF.

I. INTRODUCTION

SOME facilities used for the interim storage of spent nuclear fuel, i.e., ponds and wet silos, were not designed to modern standards and, consequently, radioactivity has leaked from them to ground [1]. This migratory contamination poses a risk to groundwater, public health, and the environment. As a consequence, investigations are necessary to locate it in order to better understand its transport and fate, the associated radiological risk, and to inform site remediation programs.

Often, best practice to assess such situations includes the installation of monitoring wells or boreholes to enable groundwater sampling campaigns and subsequent radiological analysis. Such boreholes usually extend into the ground to intersect the groundwater table and can have, for example, a slotted screen section at a specific depth to allow the water to flow in. Samples are then collected from these penetrations and sent for laboratory analysis; the latter can comprise purification to isolate a target radionuclide followed by spectroscopy.

Manuscript received 21 June 2023; revised 15 August 2023; accepted 15 September 2023. This work was supported in part by the National Nuclear Laboratory (NNL) and in part by Sellafield Ltd. (U.K.) through the EPSRC Program “TRANSCEND” (TRANSformative Science and Engineering for Nuclear Decommissioning) under Grant EP/S01019X/1. The work of Malcolm J. Joyce was supported by the Royal Society through the Wolfson Research Merit Award.

Soraia C. Elísio, Manuel Bandala, and Malcolm J. Joyce are with the School of Engineering, Lancaster University, LA1 4YW Lancaster, U.K. (e-mail: s.elisio@lancaster.ac.uk; m.joyce@lancaster.ac.uk).

Aliyu Bala was with Hybrid Instruments Ltd., LA1 4YW Lancaster, U.K. He is now with Createc Ltd., Cockermouth, CA13 0HT Cumbria, U.K.

James Graham is with the National Nuclear Laboratory, Workington, CA14 3YQ Cumbria, U.K.

Alex Grievson was with Hybrid Instruments Ltd., LA1 4YW Lancaster, U.K. He is now with ???

Color versions of one or more figures in this article are available at <https://doi.org/10.1109/TNS.2023.3319540>.

Digital Object Identifier 10.1109/TNS.2023.3319540

52 However, such sampling can be laborious and can result in
 53 secondary wastes, whereas, in areas with high dose rates, it can
 54 present radiological risks that might be avoided otherwise;
 55 neither is it ideal where wells are susceptible to drying out
 56 as the opportunity for sampling can then be lost.

57 Borehole logging is an alternative to sampling to assess
 58 radioactivity in the ground and has the potential to provide
 59 an in situ, continuous, and real-time assessment of radioactive
 60 source distributions. In this context, logging might comprise
 61 recording ionizing radiation characteristics as a function of
 62 depth in a monitoring well. However, since it was pioneered
 63 for geophysical prospecting [2], most reported works have
 64 focused on an *active* application in which radioactivity is used
 65 as a tool rather than being the objective of the assessment. The
 66 *passive* assessment of land contaminated with radioactivity via
 67 boreholes has received less attention, with works focusing on,
 68 for example, the correlation between measurements made on
 69 core samples and in boreholes [3]; spectral-shape distinction of
 70 cesium-137 and cobalt-60 [4]; high-resolution logging systems
 71 [5], [6]; and the analysis radial distributions of cobalt-60 from
 72 buried corrosion [7].

73 Passive borehole measurements can be made either by
 74 stepwise recording, while a measurement probe is stationary at
 75 selected depths (such as at the water table level for example),
 76 or by lowering the probe gradually into a well. In the former,
 77 the probe is in direct contact with contamination that might
 78 be entrained within water in the well; in the latter, the con-
 79 tamination is present in the ground (or within ground fluids)
 80 surrounding the borehole and does not have to be in direct
 81 contact with the probe. However, several limitations remain
 82 concerning, for example, the easy recovery of energy spectra
 83 with depth information that is accurate and consistent.

84 This article describes the design and test of a logging
 85 probe [8] and an associated method to infer the depth of a
 86 source of radiation in a borehole environment. A computer-
 87 implemented method to locate radioactivity in blind tubes
 88 is presented, which combines the direct detection of the
 89 cesium-137 ^{full-energy peak} ~~photopeak~~ with an application of an astrophysical
 90 seeing formalism. This is used to derive individual, radioactiv-
 91 ity depth-profile trends and, hence, enables an estimate for the
 92 depth of isolated radioactivity in a laboratory-based, borehole
 93 analog to be inferred.

94 II. BACKGROUND

95 The radiation detected with in situ detector probes in
 96 boreholes on land contaminated by products of the nuclear
 97 fuel cycle usually comprises γ rays (due to their characteristic
 98 penetrative strength and the prominent yield of γ -emitting
 99 fission products such as cesium-137) and X-rays by way
 100 of bremsstrahlung from high-energy β particles from the
 101 decay of prominent β -emitters, such as strontium-90. These
 102 photons contribute to characteristic, energy-specific lines in
 103 a spectrum (full-energy peaks), the Compton background
 104 because of scattering, and the lower-energy X-ray region due
 105 to bremsstrahlung.

106 The volume investigated in situ approximates typically to
 107 a sphere centered on the sensitive volume of the detector
 108 in use. The radius of this sphere (corresponding to the

109 depth of investigation) varies with photon energy and the
 110 interaction properties of the associated media, i.e., reducing
 111 with decreasing photon energy and increasing atomic number
 112 of the intervening media. The finite size of the detector may
 113 introduce variance from this spherical approximation, and it
 114 is anticipated that the properties of the materials constituting
 115 the monitoring system and borehole structure can influence
 116 the detected bremsstrahlung yield.

117 Sensors used in logging probes have included gas-filled
 118 detectors (Geiger-Müller tube—GM), scintillators (such as
 119 thallium-doped sodium iodide—NaI:TI), and semiconductors
 120 (i.e., high-purity germanium detectors—HPGe), yielding
 121 a range of capabilities from pulse-counting through to
 122 spectroscopy. The data from deployment are often presented
 123 as a γ -ray depth profile in terms of dose intensity, i.e., total
 124 counts, or the proportion of the total γ radiation detected
 125 associated with a particular energy (and therefore a specific
 126 radionuclide) as a function of depth in the ground, where
 127 spectroscopy allows.

128 γ -ray spectroscopy data accrued as a function of depth are
 129 generally more complex than dose or gross count data since
 130 they contain more detailed information. This might comprise
 131 a first profile based on a total γ -ray log (the sum of all types
 132 of radiation contributions) and a second profile of calculated
 133 abundancies associated with the radiation from each isotopic
 134 contribution. Such a dataset might provide information about
 135 spatial distributions of leaks in the ground as a function
 136 of depth. The output data can also be presented as a time
 137 series, where the logging probe is fixed at a specific depth,
 138 recording at different times of the year. These data may
 139 provide information about, for example, the temporal flow of a
 140 radioactivity migrating in the vicinity of the borehole. A space-
 141 time compilation of datasets, as well as measurements with an
 142 array of monitoring wells, can be essential to monitor local and
 143 site-wide mobilization or the remobilization of leaks.

144 Often, downhole γ -ray logging surveys are conducted in
 145 blind tubes, which, although having advantages over sam-
 146 pling methods that require subsequent laboratory analysis,
 147 can be challenging due to deployment constraints, limitations
 148 of the sensing apparatus, and radiological restrictions where
 149 they arise. For example, long-established boreholes on some
 150 nuclear sites are lined with carbon steel and can have screen
 151 depths of up to 10 m below ground level. They are often
 152 blinded (i.e., end-capped and thus sealed) to ensure that
 153 direct contact of the probe with the contamination surrounding
 154 the blind tube is prevented. While desirable operationally,
 155 this arrangement complicates the detection of radiations from
 156 α - and β -emitting radionuclides (notwithstanding the potential
 157 for bremsstrahlung from the latter). Furthermore, a typical tube
 158 radius of ~ 75 mm can limit the range of probes that will
 159 fit, recognizing that some radial margin is essential given the
 160 imperative that probes do not become stuck while in use.

161 Anthropogenic radioactivity in the ground is often dom-
 162 inated by cesium-137 and strontium-90, and the latter's
 163 daughter, yttrium-90. Hence, a system providing dual detection
 164 and discrimination of these radionuclides via their photon
 165 spectra can have advantages over dose-rate-only datasets.
 166 Empirical fitting procedures can be necessary to extract such

167 spectroscopic features consistently across many spectra and
 168 to extract the corresponding depth of contamination from the
 169 depth profile: this is the focus of this work.

170 III. METHOD

171 A. Photopeak Fitting

172 γ -ray spectra arising from measurements in boreholes can
 173 require a model to cater for contributions comprising, for
 174 example, a *first* source of radiation that can be somewhat
 175 discrete (the predominant radionuclide) and a *secondary*, more
 176 continuous contribution representative of a relatively complex
 177 background.

178 Cesium-137 is relatively straightforward to quantify given
 179 its 662-keV photopeak; a region-of-interest (ROI) in the energy
 180 spectrum can be selected between lower L and upper U
 181 energies defined to encompass this. The number of counts
 182 within this region is obtained by summing the counts in this
 183 histogram or (better) by fitting and integrating the mathemat-
 184 ical function that best describes it. The latter is usually a
 185 Gaussian, depending on the complexity of the spectrum.

186 In addition to the contributions to γ -ray spectra that arise
 187 due to photoelectric absorption and the incomplete interac-
 188 tions of photons subsequently escaping the detector crystal,
 189 bremsstrahlung arising from β -particle interactions in a steel
 190 blind-tube liner might also be characterized.

191 The semiempirical model applied previously for peak-shape
 192 analysis of multichannel pulse-height spectra from high-
 193 resolution germanium γ -ray detectors [9], [10], [11], [12] has
 194 been adopted here to describe and quantify spectra in the
 195 vicinity of a peak from a cerium bromide (CeBr_3) scintillator,
 196 as per the function, f , represented by a sum of terms defined
 197 as follows:

$$198 \quad f(x) = G(x) + S(x) + T(x) + b \quad (1)$$

199 where x is the abscissa corresponding to photon energy;
 200 $G(x)$ is the Gaussian function representing the photopeak;
 201 $S(x)$ represents a step discontinuity that may appear in the
 202 continuum below the Gaussian peak on its low-energy side;
 203 $T(x)$ represents the exponential trend in counts that may
 204 appear in the continuum below the Gaussian peak, again,
 205 on its low-energy side; and b is an offset corresponding to
 206 the residual background level.

207 $G(x)$ is defined in (2) where A is the amplitude of the
 208 Gaussian function, μ is the mean, and σ the standard deviation

$$209 \quad G(x) = Ae^{-\frac{(x-\mu)^2}{2\sigma^2}}. \quad (2)$$

210 $S(x)$ is defined as per (3) where B is the step function
 211 amplitude (expressed as a fraction of A) and $\text{erfc}(x)$ is the
 212 complementary error function, and the tail function, $T(x)$, is as
 213 per (4), where C is the tail function amplitude (expressed as
 214 a fraction of A) and m is the slope of the exponential

$$215 \quad S(x) = AB\text{erfc}\left(\frac{x-\mu}{\sigma\sqrt{2}}\right) \quad (3)$$

$$216 \quad T(x) = ACe^{\frac{x-\mu}{m\sigma}}\text{erfc}\left(\frac{x-\mu}{\sigma\sqrt{2}} + \frac{1}{m\sqrt{2}}\right). \quad (4)$$

217 The contribution due to the principal radionuclide over a
 218 complex continuum background of radiation is then calculated
 219 using (5), where N is then the number of counts corresponding
 220 to the photopeak, obtained by calculating the area under the
 221 Gaussian, $G(x)$

$$222 \quad N = \int_{\mu-n}^{\mu+n} G(x)dx \quad (5)$$

223 wherein n assumes a predetermined constant value indicative
 224 of a photon-energy interval sufficient to cover 3σ either side
 225 of the photopeak and the uncertainty in the N measurement
 226 is obtained by error propagation considering the obtained
 227 standard deviation in the fit variables (from the covariance
 228 matrix).

229 B. Modeling γ -Ray Log Depth Profiles

230 The response of a γ -ray logging tool can be represented as
 231 the total number of detected γ -ray counts due to the γ -emitting
 232 radioactive material present in the volume of investigation or in
 233 terms of the constituent proportions derived from analysis of a
 234 corresponding γ -ray spectrum. The contribution of individual
 235 isotopes can be evaluated and plotted as a function of depth
 236 from this analysis, yielding depth profiles for specific γ -ray
 237 lines.

238 Typically, a pulse function can be used to represent the
 239 variation in response intensity of the logging γ -ray tool as
 240 a function of depth in the vicinity of a radioactive anomaly in
 241 the ground. This can be interpreted in terms of the hypothetical
 242 response of a point detector at an infinitely slow logging speed
 243 (depth series) for a uniform zone of contamination. However,
 244 the boundaries of a pulse may not be defined sharply and
 245 pulses may have irregular shapes due to factors such as logging
 246 speed and measurement time, the size of the sensitive volume
 247 of the detector, variation of the spatial distribution of the
 248 source radioactivity in the bed formation, and changes in the
 249 volume of investigation from one measurement to another.

250 Logging tools are often used in boreholes in radioactive
 251 areas to locate contamination zones and to determine the
 252 distribution of migrating radioactivity from a source, as well
 253 as to identify and obtain relative proportions of specific
 254 nuclides within a given medium. These objectives can require
 255 careful analysis of the overall shape of the depth profile in
 256 specific regions where changes in intensity, corresponding to
 257 radioactive anomalies, are to be resolved to a sufficient degree.

258 Changes in shape of the intensity profile can be due to a
 259 combination of influences such as changes in activity, source
 260 dispersion, and the geometry of shielding materials. A source
 261 of radiation in a medium can be theorized as an extended
 262 homogeneous layer with a notional volume (extended depth
 263 vertically and horizontally relative to the orientation of the
 264 borehole) or as a point source (such as a ‘‘hot’’ particle)
 265 at a vertical/horizontal position to the borehole), as well as
 266 heterogeneous sources comprised of various point sources at
 267 different positions but within a defined volume [4]. In practice,
 268 the distribution of radioactivity in the ground is often complex
 269 and may comprise several configurations.

270 A scenario approximating to a point source in the ground,
 271 assessed with a single transit of logging system across a

range in depth spanning the position of the source, might yield a single peak shape that can be described by simple model with a small number of fitting parameters. A 1-D, PSF is an attractive option for the analysis of discrete photon depth spectra profiles of a point source near to a blind tube. However, such a function should encompass the entire activity profile, including an inner zone (corresponding to the core of the profile) and an outer zone with low numbers of counts present in its “wings.” While a Gaussian distribution might serve as a first approximation, the extremities of a profile can be more extensive than this is able to fit self-consistently. This introduces important uncertainties as to the depth at which a radioactive anomaly is discernible from the ambient.

An alternative to a Gaussian is the Moffat peak-like distribution because this accounts for the departure from Gaussian shape in the extremities on either side of the peak. A Moffat distribution is a Lorentzian continuous probability distribution modified with a variable power index. It is often described as a special case of the multivariate student- t distribution, specifically a distribution of a bivariate random variable (x, y) centered at zero (or as of the corresponding radius in this context). It has been used in astrophysics applications [13] to cater for seeing effects (see the following) in stellar profiles and for synapse image analysis concerning the nonuniform scattering of photons across the brain/cranial window of mammals [14].

In astronomy, “seeing” refers to image degradation of an astronomical object caused by atmospheric turbulence [13]. This results in brightness distributions (or radial intensity profiles) in captured, 2-D, ground-based images. Such abnormal radial intensities can manifest as irregular wings in the point-spread profiles that neither Gaussian nor Lorentzian distributions reproduce consistently, whereas a Moffat PSF can.

The standard, 2-D, Moffat PSF characterizes a spatial distribution of photons under the assumption of circular symmetry, i.e., a circular aperture, centered at the object centroid, as per g , where

$$g(x, y) = I \left[1 + \frac{(x - p_x)^2}{w_x^2} + \frac{(y - p_y)^2}{w_y^2} \right]^{-\beta} \quad (6)$$

where x and y in this context denote position, I is the amplitude, and p_x and p_y denote the centroid position of the profile in the image. The parameters w_x , w_y , and β account for the effect of photon scattering in a medium between the object and the detector recording the image, often referred to as seeing parameters that govern the width and the shape of a profile, respectively: w is a scale parameter that determines the width of the distribution and radius of a circle ($w = w_x = w_y$) in a 2-D image projection as per Fig. 1(a); β parameterizes the extent of the wings on either side of the peak of the distribution, correcting the anomalous slope for larger radii. Note that larger values of β result in a steeper slope and, when $\beta \rightarrow \infty$, the function tends to a Gaussian. Radii in one axis projection can be calculated from the full-width-at-half-maximum as equal to $(\text{FWHM}/2) = 2w(2^{1/\beta} - 1)^{1/2}$ or the full-width-at-tenth-maximum as equal to $(\text{FWTM}/2) = 2w(10^{1/\beta} - 1)^{1/2}$, based on the chosen percentage of the amplitude signal (desired level of significance). The parameter β influences the resulting radius.

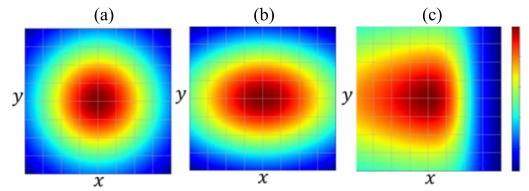


Fig. 1. Computer-generated images with color schemes representing the varying intensity levels across (x, y) coordinates for (a) symmetrical, (b) elliptical, and (c) asymmetric 2-D Moffat PSFs.

Population studies of dense stellar fields have proposed the use of modified 2-D Moffat PSFs because the spatial brightness of these distributions exhibits a degree of asymmetry. Analytically, this arises because, for elliptical dispersion, the parameter width is no longer equal for x - and y -projections (and thus $w_x \neq w_y$), as per Fig. 1(b), where the semi-major and the semiminor axes (w_x, w_y) are referenced to the central coordinates of the corresponding ellipse (x_0, y_0) . The FWHM varies symmetrically for each axis projection and at any specific inclination angle with the x -axis [15]. Asymmetry in a single-axis projection can be introduced via a position-dependent function in the corresponding width parameter w_x given by a sigmoid-type function $s(x) = 2w_x/(1 + e^{\gamma(x-x_0)})$ for x -axis asymmetry (on the y -axis, the profile is symmetrical). This asymmetric, 2-D, Moffat PSF represents a complex nonelliptical object [16] [see Fig. 1(c)] where $w_x \neq w_y$, and γ regulates the skewness of the peak profile.

Considering the photon dispersion depth profile of a vertical, 1-D scan of the simplest, point radioactive source distribution, a 1-D PSF is sufficient. Any eccentricity in the wings (corresponding to a contaminated zone boundary) is characterized by a Moffat PSF; any asymmetry is accounted for via an additional factor to yield a revised expression for g as per

$$g(x) = I \left[1 + \frac{(x - p_x)^2}{\left(\frac{2w_x}{1 + e^{\gamma(x-p_x)}} \right)^2} \right]^{-\beta} \quad (7)$$

where γ can be positive or negative, to indicate skew to the lower and higher values of a depth maximum, respectively, and null if symmetric, with β and w_x defined as positive. Higher values of β indicate a higher slope of the distribution wings, and higher values of w_x indicate a wider distribution. Note that the calculation of FWHM is more complex in non-symmetric cases, as an explicit isolated solution for $(x - p_x)$, and the determination of the radius (in a x -axis projection) requires the application of numerical methods, such as the Newton–Raphson method [17]. However, in instances where the fit yields a very small γ value, the previous FWHM expression can be employed for a quick assessment of the spread. This simplified scenario is used to define baseline values for γ , β , and w_x . Any detraction from these baseline values might suggest an extended or multicomponent source of radioactivity or discrepancies due to photon scatter arising due to density or structural changes of the ground surrounding a given borehole.

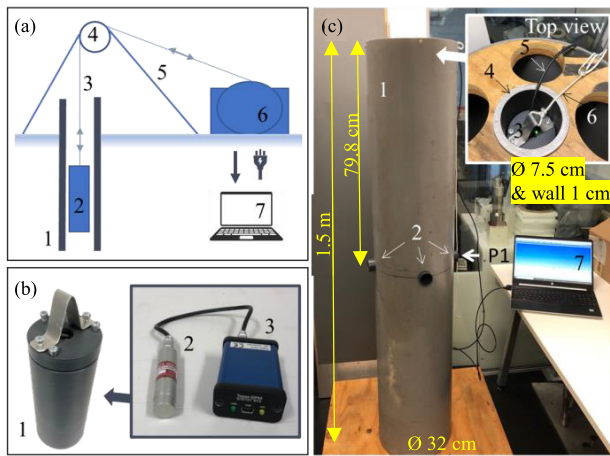


Fig. 2. (a) Schematic of the approach showing the borehole (1), the probe (2), tether (3), the pulley unit of the deployment system (4 and 5), and the winch (6) and laptop (7). (b) ABACUS probe unit (size $\text{Ø}7 \times 20$ cm) (1) including the detector (size $\text{Ø}1.5 \times 6.5$ cm) (2) and MCA (size $7 \times 4.5 \times 2.6$ cm) (3). (c) Laboratory setup including the testbed (1), the source ports (2), and the top view of the unit.

IV. MATERIALS AND METHODS

A. Blind-Tube Logging Probe Prototype

The blind-tube logging probe (BLP) used in this work, “ABACUS”, as per Fig. 2, comprises a γ -ray spectrometer and a digital multichannel analyzer (MCA) in an outer, cylindrical case. The spectrometer is made up of an inorganic scintillation detector and a silicon photomultiplier (SiPM) in a cylindrical, compact (physical size of $\text{Ø}1.5 \times 6.5$ cm²) hermetic unit (VS-1402-20, commercialized by Scionix, Netherlands). The scintillator is a $\text{Ø}9.5 \times 10$ mm² CeBr₃ crystal, and the crystal readout is a 6×6 mm² PM6660-SiPM (Ketek GmbH, Germany). The SiPM output is conditioned by a built-in preamplifier to cater for the effect of temperature; the influence of temperature on its light output was not catered for recognizing that the measurements were performed in a laboratory with some temperature compensation. Cerium bromide provides competitive γ -ray detection efficiency (with an effective atomic number, Z_{eff} , of 46, and a density of the material, ρ , of 5.2 g/cm³), energy resolution (3.2%–4% at 662 keV), high-count-rate capability (decay time = 17 ns), and radiation hardness ($<10^5$ Gy) [18].

The MCA used in ABACUS is a Topaz-SiPM supplied in a rugged and pocket-size (physical size of $7 \times 4.5 \times 2.6$ cm³) aluminum box with input and output connectors (commercialized by BrightSpec NV). It is among the smallest, full-featured MCAs currently available and performs pulse-height analysis of the signal from the scintillation detectors to provide energy spectra. It operates on a 5-V low-ripple, low-noise supply for the detector and can be interfaced to a laptop or notebook easily via USB 2.0 communication interface for power supply and data transfer. The unit includes a spectroscopy software interface. Note that by installing the MCA unit in the probe case, the detector output signal is digitalized before being sent to the surface, enabling signal transmission with less noise, distortion, and environmental interference [9].

The probe case has a simple cylindrical geometry and physical dimensions compatible with the dimensions of existing blind tubes. The γ -ray spectrometer is fixed parallel to

the central axis of the case and centered at the bottom. A collimator is not used, and hence, the detection response is assumed isotropic apart from the top side of the crystal where the electronics is housed. The signal processing module is placed on top of the detector and connected to it via a LEMO¹ connector. The case is made of plastic ($\text{Ø}70 \times 211$ mm long) with a top lid with a hole for the USB cable and a hook to aid deployment and recovery when in use.

B. Deployment System

A typical deployment system for the ABACUS probe comprises a winch by which the tool is lowered and retrieved, a sheave to add the change of the direction of the cable between the winch and the hole, and a high-resolution encoder for depth measurement. Typical logging cables (multicore wired) provide a combined means of data transfer, power supply, and mechanical support. Surface instruments, comprising a data logger or control unit, store the data and are used to control the winch system, to set the position of the probe within a borehole.

In the context of this work, a simplified deployment system has been used for laboratory-based tests in which a sheave and encoder are not used, with the probe lowered/raised manually with depth position measured using a hand-held, laser-based distance meter at the top of the blind tube. The logging cable then consists of two separate cables: a rope to support the weight of the probe and a 3-m-long USB cable for data transmission and power supply.

C. Blind-Tube Testbed

The blind-tube testbed used in this research is a laboratory-controlled monitoring well designed for radiation detection and photon depth-profile testing. It has been designed to calibrate the BLP response for a variety of scenarios (e.g., simple-to-complex spatial distributions of source and media) before conducting field measurements.

The testbed comprises an inner, vertical pipe at the center of an outer pipe fixed in a base, with four smaller tubes intersecting both pipes horizontally, fixed 80 cm from the top. The inner pipe represents the blind tube in this arrangement with the material and size of this pipe selected to replicate legacy blind tubes at nuclear sites, i.e., Sellafield, as close as possible; in this case, blind tubes lined with carbon steel with inner diameters ranging from 75 to 80 mm and wall thicknesses ranging from 6 to 10 mm. The carbon steel tube (European Tubes Ltd., U.K.) is 1.5 m long with an inner diameter of 75 mm and a wall thickness of 9.5 mm. The outer pipe functions as a material retainer or tank. It is 1.5 m long, 320 mm in diameter, made of plastic, and designed so that the space between the blind tube and the plastic outer pipe can be filled with material (such as sand) to recreate a vertical ground core, translating to about 113 mm of material surrounding the blind tube (not done in this work). The horizontal tubes create a void in the matrix material to enable sealed radioactive sources to be inserted and removed quickly and easily.

In this research, a scenario has been assumed comprising a single point source with the least degree of scattering possible

¹Registered trademark.

464 between source and detector, with the test pit left empty of
 465 material and a sealed source fixed close to the wall of the
 466 blind tube.

467 D. Experimental Method

468 A cesium-137 source with an activity of 304 kBq was
 469 inserted into the horizontal tube at position P1 (see Fig. 2). The
 470 BLP prototype was then lowered into the blind-tube testbed
 471 (described above) and fixed at various depth positions using
 472 a rope attached to the top of the testbed. The position of the
 473 probe in the pipe, d , relative to the top of the testbed, was
 474 determined using a hand-held laser position meter. The meter
 475 was placed on top of the tank, with its laser output directed
 476 downward toward the top surface of the logging probe.

477 These data were then converted into distance, D , between
 478 the top of the pipe and the center of the sensor element
 479 by considering the internal dimensions of the probe. Each
 480 spectrum was acquired for 1 h to achieve sufficient statistical
 481 precision for peak evaluation. The data were transferred via
 482 USB 2.0 to a laptop running the γ -ray spectroscopy software,
 483 and each spectrum was saved in the text file format. The
 484 following sections describes an algorithm written in python²
 485 used to analyze each obtained spectrum for a variety of depth
 486 positions.

487 E. γ -Ray Spectral Log Analysis

488 The analysis was divided into two stages. The photopeak
 489 model (1) is used first to characterize the γ -ray spectra
 490 recorded by the BLP. Each spectrum is the energy distribution
 491 of the photons (γ rays and X-rays) determined at a specific
 492 depth within the blind-tube testbed as per Fig. 3. Second, the
 493 depth profile fit is performed as per Fig. 4.

494 The photopeak model has been applied to each spectrum for
 495 each depth position, i , where increasing values of i correspond
 496 to increasing depth into the ground or, in this case, the testbed.
 497 An ROI defined between a lower L and upper U energy
 498 bounds is selected to initialize the method encompassing a
 499 peak, i.e., the 662-keV line of cesium-137. Initial U and L
 500 values were derived from a typical spectrum: L to the right of
 501 the Compton edge and U to the right of the photopeak where
 502 the count level approaches the level of background noise.

503 Least-squares minimization was used to optimize the fit
 504 of f [see (1)] to the data within the ROI at each depth i . The
 505 fitting algorithm starts with an initial fitting iteration to obtain
 506 initial values for the fit parameters (derived from a typical
 507 spectrum) and this is then optimized to obtain the parameters
 508 and their associated uncertainties. These values are saved, and
 509 the process is repeated for the next position. The method
 510 checks for errors in the fitting process (such as a failure of
 511 the fit or to find optimal parameters), adjusts where necessary,
 512 and repeats the process.

513 The ROI may be adjusted by reducing U by one channel to a
 514 lower energy until it equals μ (the centroid of the Gaussian).
 515 If the process still fails to fit the data, an error message is
 516 registered (since effectively no photopeak is detected) and the
 517 method moves on to the next position. Following the fitting

²Trademarked.

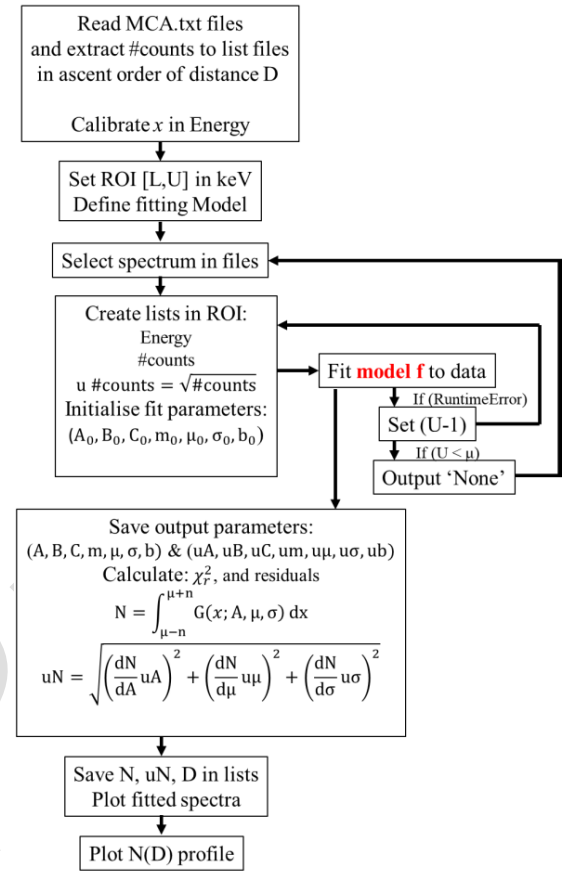


Fig. 3. Flowchart of the spectrum fitting process including the data flow.

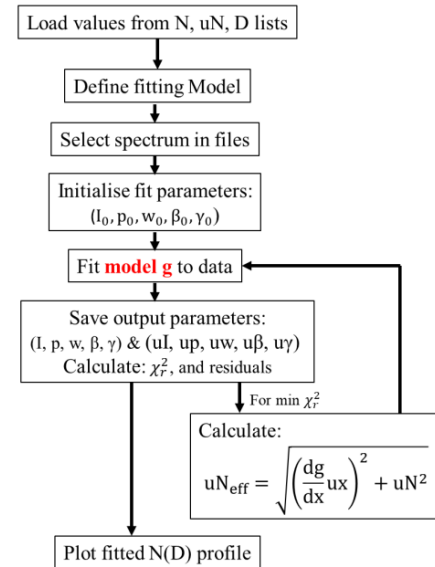


Fig. 4. Flowchart of the depth-profile fitting process.

518 process, (5) is used to calculate the total number of counts N_i 518
 519 corresponding to a number of counts under the photopeak, i.e., 519
 520 indicative of the level of cesium-137 662-keV γ rays detected 520
 521 at each position i . 521

522 The aim of the fitting process is to find values of 522
 523 unconstrained parameters based on a minimization using a 523
 524 Levenberg–Marquardt algorithm. In python, this is performed 524
 525 by the function `scipy.optimize.curve_fit()`; a chi-squared test of 525
 526 independence is used to assess the consistency of a given fit. 526

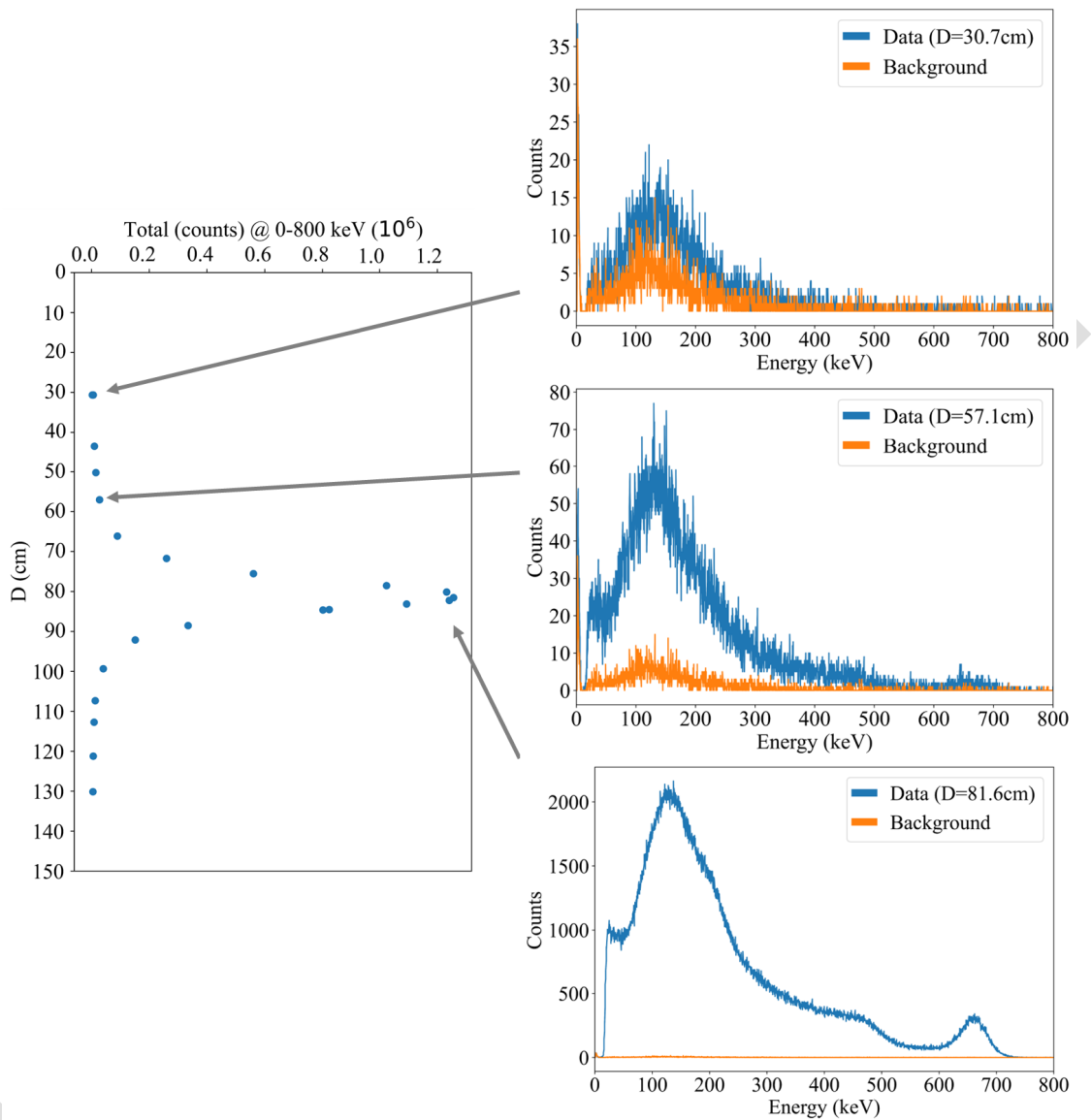


Fig. 5. Depth versus total counts for a single profile exercise (left) and example spectra for three different positions (right): 30.7, 57.1, and 81.6 cm.

V. RESULTS AND DISCUSSION

The γ -ray spectra obtained with cesium-137 at P1, and with the BLP prototype positioned at specific distances 30 up to 130 cm from the top pipe, are shown in Fig. 5. This illustrates that the intensity of the 662-keV peak is greater when the detector is close to the source and decreases when it is further away, as expected, with the highest intensity observed at the shortest possible source–detector separation. A wide scatter continuum is observed due to the effect of the surroundings and incomplete photon absorption in the detector crystal.

The sum of counts may be obtained by direct summation or by fitting an analytical function to the data. A Gaussian with an additional component to represent the low-energy tailing on the peak, f , was used, as per (1), with parameters as defined earlier. χ_v^2 for the fits was ~ 1 , but the algorithm fails to fit peaks of small amplitude (< 15 counts). This error arises from the failure of the optimization algorithm to achieve convergence within the specified number of iterations and may be attributable to the model’s complexity and the presence

of noise on a low amplitude photopeak. Note that applying moderate smoothing techniques, such as the Savitzky–Golay filter [19], on spectra with low photopeak amplitudes prior to optimization process may address this issue and, consequently, enhance the accuracy of the profile encompassing the limits of the γ -ray depth profile (not done in this work). Fig. 6 shows an example of a fit for cesium-137. The number of counts under the peak N_p was extracted by integrating the Gaussian component of the optimized function (1), between 3σ on either side of the μ -peak value, plotted against the detector position in the blind-tube testbed, as per Fig. 6. These data describe an asymmetric PSF akin to astrophysical problems and have been fit with a Moffat function, g , with a skew component, as per (7), where the parameters are as defined earlier. Fig. 6 suggests an acceptable fit incorporating the asymmetric trend, which is superior when compared to Gaussian-type models (see Table I).

The amplitude term, I , can be used to estimate the activity or concentration of cesium-137 in the sample, provided that

527

528

529

530

531

532

533

534

535

536

537

538

539

540

541

542

543

544

545

546

547

548

549

550

551

552

553

554

555

556

557

558

559

560

561

562

563

564

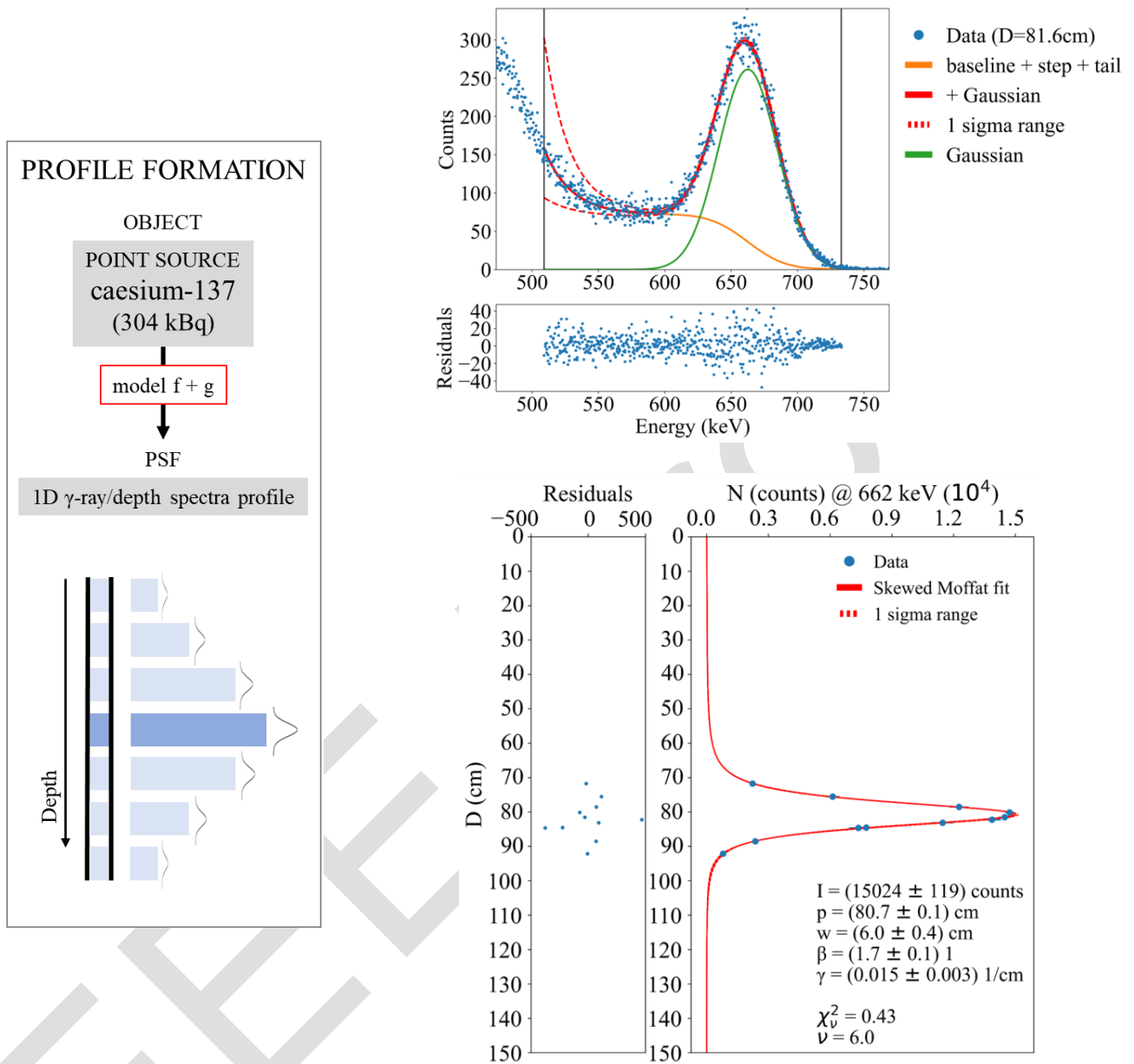


Fig. 6. Schematic of the depth profiling process (left) with an example spectrum (right, top) including the combination of fits comprising (1) and the depth profile obtained from an experimental scan (right, bottom) with the modified Moffat PSF fit as per (7), with the corresponding fit parameters: I represents the amplitude, p is the peak depth position, w refers to the width, β refers to the shape, and γ refers to the skewness term of the profile. The reduced chi-squared, χ^2_ν , was 0.43, with the number of degrees of freedom (ν) of 6.

TABLE I
PSF MODELS AND FIT PARAMETERS

Parameter	Gaussian	Skewed Gaussian	1-D Moffat	1-D Skew Moffat
A / counts	14493 ± 397	11806 ± 1569	14924 ± 209	15024 ± 119
μ / cm	80.5 ± 0.3	78 ± 1	80.5 ± 0.1	80.7 ± 0.1
σ / cm	4.3 ± 0.2	5.3 ± 0.7	7.1 ± 0.8	6.0 ± 0.4
β	-	-	2.2 ± 0.3	1.7 ± 0.1
γ / cm^{-1}	-	1.0 ± 0.5	-	0.015 ± 0.003
χ^2_ν	12.8	12.5	1.7	0.4
df	8	7	7	6

565 calibration is performed. The maximum peak height observed
 566 in this work was (15024 ± 119) cph (~ 4 cps) for a ^{137}Cs
 567 point source of activity of 304 kBq.

The position of the source is inferred from the fit in
 Fig. 6 associated with the centroid parameter-, p , to give
 (80.7 ± 0.1) cm. P1 was positioned at (79.8 ± 0.5) cm,

568
 569
 570

highlighting a consistent result within the uncertainties (relative error $\sim 1\%$).

The width term, w , can be used to estimate the vertical spatial resolution of the system defined at 50% of the signal and given approximately by $2w_x(2^{1/\beta} - 1)^{1/2}$, i.e., (8.5 ± 0.6) cm.

The shape terms β and γ determine the rate of change of the width of the distribution (spread of radiation) in relation to the peak position p along the x -axis. These suggest a relative degree of attenuation that photons experience before reaching the sensor, influenced by factors such as shielding or the density of the surrounding media. Since, in this study, the setup was designed to minimize attenuation, the values obtained correspond to this scenario, as per (1.7 ± 0.1) and (0.015 ± 0.003) cm^{-1} for β and γ , respectively, and are intrinsic to this blind-tube testbed and detector system arrangement. Moreover, the γ value obtained is positive, very small but nonzero, indicating a slight asymmetry in the distribution (steeper on the right side of the peak centroid than the left). This effect may be due to an asymmetric attenuation, i.e., the presence of sensor case, electronics, and the length of the probe case where the MCA is positioned, on the back of the sensor crystal.

By analyzing the parameters (I , p , w , and β) and their corresponding three-standard deviations in both nonskewed and skewed Moffat models (Table I), the results indicate that all the corresponding parameters are similar within the 99.7% confidence range. This implies that the models yield similar fits to the data distribution, which is reasonable given that the obtained γ value is close to zero.

VI. CONCLUSION

In situ borehole monitoring of radioactivity is an important modality by which both the location and the composition of radioactive contamination entrained in groundwater and geological strata can be probed. However, photon spectra arising from this approach can be complex and varied, and hence, reliable analytical methods are necessary by which individual contributions to them can be estimated. Likewise, the point-spread distribution of photon count data that can arise with depth concerning a particular anomaly can be asymmetric due to inhomogeneities in the borehole surroundings and the influence of the monitoring instrumentation on scatter while in use underground.

In this research, the design and development of a prototype borehole monitoring probe and bespoke testbed have been described. The use of these is demonstrated in which the semiempirical model developed by Phillips and Marlow [9] has been combined with development of the Moffat PSF [13] to extract spectroscopic features and localization information, respectively. This approach, combined with the ABACUS BLP, yields a consistent indication of the depth of radioactive source positioned in a bespoke, blind-tube testbed. In future, these approaches will be targeted toward understanding more complicated source distribution scenarios, the proportion and spatial distribution of ^{137}Cs and ^{90}Sr in aqueous media, and progressing to active testing in the field.

ACKNOWLEDGMENT

The authors acknowledge useful discussions with B. Greenhalgh and T. Calverley.

REFERENCES

- [1] P. Hallington, J. Heneghan, and J. Graham. (2021). *RemPlex Summit Case Studies: Optimization of Remediation Planning Approaches Based on Lessons Learned at the Sellafield Site, U.K.* Accessed: May 4, 2022. [Online]. Available: <https://www.pnnl.gov/projects/remplex/case-studies#CaseStudy4>
- [2] J. Homilius and S. Lorch, "On the theory of gamma ray scattering in boreholes," *Geophys. Prospecting*, vol. 6, no. 4, pp. 342–364, 1958.
- [3] H. L. Nguyen et al., "Analysis of the relationship binding in situ gamma count rates and soil sample activities: Implication on radionuclide inventory and uncertainty estimates due to spatial variability," *J. Environ. Radioactivity*, vol. 192, pp. 349–361, Dec. 2018.
- [4] R. D. Wilson, C. J. Koizumi, J. E. Meisner, and D. C. Stromswold, "Spectral shape analysis for contaminant logging at the Hanford site," *IEEE Trans. Nucl. Sci.*, vol. 45, no. 3, pp. 997–1001, Jun. 1998.
- [5] J. R. Giles and K. J. Dooley, "High resolution gamma-spectroscopy well logging system," *J. Radioanal. Nucl. Chem.*, vol. 233, nos. 1–2, pp. 125b–130, Jul. 1998.
- [6] C. J. Koizumi, J. R. Brodeur, R. K. Price, J. E. Meisner and D. C. Stromswold, "High-resolution gamma-ray spectrometry logging for contamination assessment," *Nucl. Geophys.*, vol. 8, no. 2, pp. 149–164, 1994.
- [7] L. L. Gadeken, W. P. Madigan, and H. D. Smith Jr., "Radial distributions of ^{60}Co contaminants surrounding wellbores at the Hanford site," in *Proc. IEEE Nucl. Sci. Symp.*, vol. 1, 1995, pp. 214–218. **November**
- [8] S. Elisio and M. J. Joyce, "Method and apparatus for determining attributes of a source of radiation," U.S. Patent P 347 121GB/CAB, Sep. 29, 2022.
- [9] G. W. Phillips and K. W. Marlow, "Automatic analysis of gamma-ray spectra from germanium detectors," *Nucl. Instrum. Methods*, vol. 137, no. 3, pp. 525–536, Sep. 1976.
- [10] J. Uher, G. Roach, and J. Tickner, "Peak fitting and identification software library for high resolution gamma-ray spectra," *Nucl. Instrum. Methods Phys. Res. A, Accel. Spectrom. Detect. Assoc. Equip.*, vol. 619, nos. 1–3, pp. 457–459, Jul. 2010.
- [11] P. Mortreau and R. Berndt, "Characterisation of cadmium zinc telluride detector spectra—Application to the analysis of spent fuel spectra," *Nucl. Instrum. Methods Phys. Res. A, Accel. Spectrom. Detect. Assoc. Equip.*, vol. 458, nos. 1–2, pp. 183–188, Feb. 2001.
- [12] A. Varley, A. Tyler, L. Smith, and P. Dale, "Development of a neural network approach to characterise ^{226}Ra contamination at legacy sites using gamma-ray spectra taken from boreholes," *J. Environ. Radioactivity*, vol. 140, pp. 130–140, Feb. 2015.
- [13] A. F. J. Moffat, "A theoretical investigation of focal stellar images in the photographic emulsion and application to photographic photometry," *Astron. Astrophys.*, vol. 3, p. 455, Dec. 1969.
- [14] T. M. Ryan, A. J. Hinojosa, R. Vroman, C. Papisavvas, and L. Lagnado, "Correction of z-motion artefacts to allow population imaging of synaptic activity in behaving mice," *J. Physiol.*, vol. 598, no. 10, pp. 1809–1827, May 2020.
- [15] G. Fiorentino et al., "On the use of asymmetric PSF on NIR images of crowded stellar fields," *Proc. SPIE*, vol. 9148, pp. 1301–1314, Aug. 2014.
- [16] S. K. Jensen Jr., S. D. Brittain, J. R. Najita, and J. S. Carr, "Modeling of CO rovibrational line emission of HD 141569," *Publications Astronomical Soc. Pacific*, vol. 133, no. 1028, Oct. 2021, Art. no. 104402.
- [17] J. P. Dedieu, "Newton-Raphson method," in *Encyclopedia of Applied and Computational Mathematics*, B. Engquist, Ed. Berlin, Germany: Springer, 2015.
- [18] S. Elisio, M. J. Joyce, J. Graham, and B. Greenhalgh, "An advanced blind-tube monitoring instrument to improve characterization of sub-surface radioactive plumes," in *Proc. EPJ Web Conf.*, vol. 253, 2021, p. 08005.
- [19] A. Savitzky and M. J. E. Golay, "Smoothing and differentiation of data by simplified least squares procedures," *Anal. Chem.*, vol. 36, no. 8, pp. 1627–1639, Jul. 1964.

625
626
627
628
629
630
631
632
633
634
635
636
637
638
639
640
641
642
643
644
645
646
647
648
649
650
651
652
653
654
655
656
657
658
659
660
661
662
663
664
665
666
667
668
669
670
671
672
673
674
675
676
677
678
679
680
681
682
683
684
685
686
687
688
689
690
691
692
693

AQ:6

AUTHOR QUERIES

AUTHOR PLEASE ANSWER ALL QUERIES

PLEASE NOTE: We cannot accept new source files as corrections for your article. If possible, please annotate the PDF proof we have sent you with your corrections and upload it via the Author Gateway. Alternatively, you may send us your corrections in list format. You may also upload revised graphics via the Author Gateway.

Carefully check the page proofs (and coordinate with all authors); additional changes or updates **WILL NOT** be accepted after the article is published online/print in its final form. Please check author names and affiliations, funding, as well as the overall article for any errors prior to sending in your author proof corrections.

AQ:1 = Please confirm or add details for any funding or financial support for the research of this article.

AQ:2 = Please provide the expansion of the acronym EPSRC for your funding agency. Providing the correct acknowledgment will ensure proper credit to the funder.

AQ:3 = Please confirm whether the edits made in the past/current affiliation of all the authors are correct.

AQ:4 = Please provide the full current affiliation details (department name, name of university/institution, city, state/country, zip/postal code) for the author Alex Grievson.

AQ:5 = Please provide the appropriate section number for the phrase “following sections.”

AQ:6 = Please provide the month for Ref. [7].

Point-Spread Analysis of γ -Ray/Depth Spectra for Borehole Monitoring Applications

Soraia C. Elísio, Aliyu Bala, Manuel Bandala, James Graham, Alex Grievson,
and Malcolm J. Joyce[®], *Member, IEEE*

Abstract—An approach to the analysis of γ -ray spectra that might arise as depth profiles from the characterization of radioactivity in boreholes is described. A borehole logging probe, “ABACUS,” has been designed and constructed, which comprises a cerium bromide detector and a built-in multichannel analyzer (MCA). This has been tested in a bespoke, laboratory-based testbed built to replicate the borehole environment. An established, semiempirical model has been applied to data arising from the cerium bromide scintillation detector to extract the number of counts under the full-energy peak from each of the resulting γ -ray spectra (in this case the 662 keV line from ^{137}Cs) associated with each depth position, which also enables this information to be isolated from other contributions such as background and the Compton continuum. A complementary approach has been adopted to process the asymmetric and non-Gaussian trend that concerns the full-energy peak count as a function of depth in the borehole testbed for a given depth profile when the testbed is subject to the activity provided by a sealed, ^{137}Cs source. This comprises a modified, Moffat point-spread function (PSF). The Moffat function is a continuous probability distribution based on the Lorentzian distribution. Its particular importance is due to its ability to reconstruct PSFs that comprise wings that cannot be reproduced accurately by either a Gaussian or Lorentzian function. This application of the Moffat formalism to radioactive contamination assessment profiles enables an effective and accurate assessment to be made of the position of localized radioactivity in the testbed wall.

Index Terms— γ -ray detection, curve fitting, Gaussian distribution, nuclear measurements, radioactive pollution.

NOMENCLATURE

Glossary

- A* Amplitude of Gaussian function applied to photopeak.
- B* Amplitude of step function expressed as a fraction of *A*.
- b* Offset representing the residual background count.

- β Parameter governing the shape of a depth profile.
- C* Tail function amplitude expressed as a fraction of *A*.
- df* Number of degrees of freedom.
- f* Spectrum fitting function.
- G* Gaussian function.
- g* Moffat point-spread function (PSF).
- γ Skew parameter of the peak of a depth profile.
- I* Amplitude of a Moffat PSF.
- μ Centroid of the Gaussian function applied to photopeak.
- m* Slope of the exponential in the tail function, *T*.
- N* Number of counts in photopeak.
- n* Constant in Gaussian integral ensuring 3σ coverage.
- p* Peak depth position as per centroid components below.
- p_x Centroid in *x* of an image or depth profile.
- p_y Centroid in *y* of an image or depth profile.
- S* Step discontinuity function in photon spectrum.
- s* Sigmoid-type function describing *x*-axis asymmetry.
- σ Standard deviation of the Gaussian applied to photopeak.
- T* Tail function applied to photon spectrum.
- w_x Parameter governing the width of a depth profile in *x*.
- w_y Parameter governing the width of a depth profile in *y*.
- x_0 Central *x* coordinate of an elliptic profile.
- y_0 Central *y* coordinate of an elliptic profile.
- x* Abscissa denoting photon energy or depth.
- y* Parameter orthogonal to depth in Moffat PSF.

I. INTRODUCTION

SOME facilities used for the interim storage of spent nuclear fuel, i.e., ponds and wet silos, were not designed to modern standards and, consequently, radioactivity has leaked from them to ground [1]. This migratory contamination poses a risk to groundwater, public health, and the environment. As a consequence, investigations are necessary to locate it in order to better understand its transport and fate, the associated radiological risk, and to inform site remediation programs.

Often, best practice to assess such situations includes the installation of monitoring wells or boreholes to enable groundwater sampling campaigns and subsequent radiological analysis. Such boreholes usually extend into the ground to intersect the groundwater table and can have, for example, a slotted screen section at a specific depth to allow the water to flow in. Samples are then collected from these penetrations and sent for laboratory analysis; the latter can comprise purification to isolate a target radionuclide followed by spectroscopy.

Manuscript received 21 June 2023; revised 15 August 2023; accepted 15 September 2023. This work was supported in part by the National Nuclear Laboratory (NNL) and in part by Sellafield Ltd. (U.K.) through the EPSRC Program “TRANSCEND” (TRANSformative Science and Engineering for Nuclear Decommissioning) under Grant EP/S01019X/1. The work of Malcolm J. Joyce was supported by the Royal Society through the Wolfson Research Merit Award.

Soraia C. Elísio, Manuel Bandala, and Malcolm J. Joyce are with the School of Engineering, Lancaster University, LA1 4YW Lancaster, U.K. (e-mail: s.elisio@lancaster.ac.uk; m.joyce@lancaster.ac.uk).

Aliyu Bala was with Hybrid Instruments Ltd., LA1 4YW Lancaster, U.K. He is now with Createc Ltd., Cockermonth, CA13 0HT Cumbria, U.K.

James Graham is with the National Nuclear Laboratory, Workington, CA14 3YQ Cumbria, U.K.

Alex Grievson was with Hybrid Instruments Ltd., LA1 4YW Lancaster, U.K. He is now with ???

Color versions of one or more figures in this article are available at <https://doi.org/10.1109/TNS.2023.3319540>.

Digital Object Identifier 10.1109/TNS.2023.3319540

52 However, such sampling can be laborious and can result in
 53 secondary wastes, whereas, in areas with high dose rates, it can
 54 present radiological risks that might be avoided otherwise;
 55 neither is it ideal where wells are susceptible to drying out
 56 as the opportunity for sampling can then be lost.

57 Borehole logging is an alternative to sampling to assess
 58 radioactivity in the ground and has the potential to provide
 59 an in situ, continuous, and real-time assessment of radioactive
 60 source distributions. In this context, logging might comprise
 61 recording ionizing radiation characteristics as a function of
 62 depth in a monitoring well. However, since it was pioneered
 63 for geophysical prospecting [2], most reported works have
 64 focused on an *active* application in which radioactivity is used
 65 as a tool rather than being the objective of the assessment. The
 66 *passive* assessment of land contaminated with radioactivity via
 67 boreholes has received less attention, with works focusing on,
 68 for example, the correlation between measurements made on
 69 core samples and in boreholes [3]; spectral-shape distinction of
 70 cesium-137 and cobalt-60 [4]; high-resolution logging systems
 71 [5], [6]; and the analysis radial distributions of cobalt-60 from
 72 buried corrosion [7].

73 Passive borehole measurements can be made either by
 74 stepwise recording, while a measurement probe is stationary at
 75 selected depths (such as at the water table level for example),
 76 or by lowering the probe gradually into a well. In the former,
 77 the probe is in direct contact with contamination that might
 78 be entrained within water in the well; in the latter, the con-
 79 tamination is present in the ground (or within ground fluids)
 80 surrounding the borehole and does not have to be in direct
 81 contact with the probe. However, several limitations remain
 82 concerning, for example, the easy recovery of energy spectra
 83 with depth information that is accurate and consistent.

84 This article describes the design and test of a logging
 85 probe [8] and an associated method to infer the depth of a
 86 source of radiation in a borehole environment. A computer-
 87 implemented method to locate radioactivity in blind tubes
 88 is presented, which combines the direct detection of the
 89 cesium-137 photopeak with an application of an astrophysical
 90 seeing formalism. This is used to derive individual, radioactiv-
 91 ity depth-profile trends and, hence, enables an estimate for the
 92 depth of isolated radioactivity in a laboratory-based, borehole
 93 analog to be inferred.

94 II. BACKGROUND

95 The radiation detected with in situ detector probes in
 96 boreholes on land contaminated by products of the nuclear
 97 fuel cycle usually comprises γ rays (due to their characteristic
 98 penetrative strength and the prominent yield of γ -emitting
 99 fission products such as cesium-137) and X-rays by way
 100 of bremsstrahlung from high-energy β particles from the
 101 decay of prominent β -emitters, such as strontium-90. These
 102 photons contribute to characteristic, energy-specific lines in
 103 a spectrum (full-energy peaks), the Compton background
 104 because of scattering, and the lower-energy X-ray region due
 105 to bremsstrahlung.

106 The volume investigated in situ approximates typically to
 107 a sphere centered on the sensitive volume of the detector
 108 in use. The radius of this sphere (corresponding to the

109 depth of investigation) varies with photon energy and the
 110 interaction properties of the associated media, i.e., reducing
 111 with decreasing photon energy and increasing atomic number
 112 of the intervening media. The finite size of the detector may
 113 introduce variance from this spherical approximation, and it
 114 is anticipated that the properties of the materials constituting
 115 the monitoring system and borehole structure can influence
 116 the detected bremsstrahlung yield.

117 Sensors used in logging probes have included gas-filled
 118 detectors (Geiger-Müller tube—GM), scintillators (such as
 119 thallium-doped sodium iodide—NaI:Tl), and semiconductors
 120 (i.e., high-purity germanium detectors—HPGe), yielding
 121 a range of capabilities from pulse-counting through to
 122 spectroscopy. The data from deployment are often presented
 123 as a γ -ray depth profile in terms of dose intensity, i.e., total
 124 counts, or the proportion of the total γ radiation detected
 125 associated with a particular energy (and therefore a specific
 126 radionuclide) as a function of depth in the ground, where
 127 spectroscopy allows.

128 γ -ray spectroscopy data accrued as a function of depth are
 129 generally more complex than dose or gross count data since
 130 they contain more detailed information. This might comprise
 131 a first profile based on a total γ -ray log (the sum of all types
 132 of radiation contributions) and a second profile of calculated
 133 abundancies associated with the radiation from each isotopic
 134 contribution. Such a dataset might provide information about
 135 spatial distributions of leaks in the ground as a function
 136 of depth. The output data can also be presented as a time
 137 series, where the logging probe is fixed at a specific depth,
 138 recording at different times of the year. These data may
 139 provide information about, for example, the temporal flow of a
 140 radioactivity migrating in the vicinity of the borehole. A space-
 141 time compilation of datasets, as well as measurements with an
 142 array of monitoring wells, can be essential to monitor local and
 143 site-wide mobilization or the remobilization of leaks.

144 Often, downhole γ -ray logging surveys are conducted in
 145 blind tubes, which, although having advantages over sam-
 146 pling methods that require subsequent laboratory analysis,
 147 can be challenging due to deployment constraints, limitations
 148 of the sensing apparatus, and radiological restrictions where
 149 they arise. For example, long-established boreholes on some
 150 nuclear sites are lined with carbon steel and can have screen
 151 depths of up to 10 m below ground level. They are often
 152 blinded (i.e., end-capped and thus sealed) to ensure that
 153 direct contact of the probe with the contamination surrounding
 154 the blind tube is prevented. While desirable operationally,
 155 this arrangement complicates the detection of radiations from
 156 α - and β -emitting radionuclides (notwithstanding the potential
 157 for bremsstrahlung from the latter). Furthermore, a typical tube
 158 radius of ~ 75 mm can limit the range of probes that will
 159 fit, recognizing that some radial margin is essential given the
 160 imperative that probes do not become stuck while in use.

161 Anthropogenic radioactivity in the ground is often dom-
 162 inated by cesium-137 and strontium-90, and the latter's
 163 daughter, yttrium-90. Hence, a system providing dual detection
 164 and discrimination of these radionuclides via their photon
 165 spectra can have advantages over dose-rate-only datasets.
 166 Empirical fitting procedures can be necessary to extract such

167 spectroscopic features consistently across many spectra and
 168 to extract the corresponding depth of contamination from the
 169 depth profile: this is the focus of this work.

170 III. METHOD

171 A. Photopeak Fitting

172 γ -ray spectra arising from measurements in boreholes can
 173 require a model to cater for contributions comprising, for
 174 example, a *first* source of radiation that can be somewhat
 175 discrete (the predominant radionuclide) and a *secondary*, more
 176 continuous contribution representative of a relatively complex
 177 background.

178 Cesium-137 is relatively straightforward to quantify given
 179 its 662-keV photopeak; a region-of-interest (ROI) in the energy
 180 spectrum can be selected between lower L and upper U
 181 energies defined to encompass this. The number of counts
 182 within this region is obtained by summing the counts in this
 183 histogram or (better) by fitting and integrating the mathemat-
 184 ical function that best describes it. The latter is usually a
 185 Gaussian, depending on the complexity of the spectrum.

186 In addition to the contributions to γ -ray spectra that arise
 187 due to photoelectric absorption and the incomplete interac-
 188 tions of photons subsequently escaping the detector crystal,
 189 bremsstrahlung arising from β -particle interactions in a steel
 190 blind-tube liner might also be characterized.

191 The semiempirical model applied previously for peak-shape
 192 analysis of multichannel pulse-height spectra from high-
 193 resolution germanium γ -ray detectors [9], [10], [11], [12] has
 194 been adopted here to describe and quantify spectra in the
 195 vicinity of a peak from a cerium bromide (CeBr_3) scintillator,
 196 as per the function, f , represented by a sum of terms defined
 197 as follows:

$$198 \quad f(x) = G(x) + S(x) + T(x) + b \quad (1)$$

199 where x is the abscissa corresponding to photon energy;
 200 $G(x)$ is the Gaussian function representing the photopeak;
 201 $S(x)$ represents a step discontinuity that may appear in the
 202 continuum below the Gaussian peak on its low-energy side;
 203 $T(x)$ represents the exponential trend in counts that may
 204 appear in the continuum below the Gaussian peak, again,
 205 on its low-energy side; and b is an offset corresponding to
 206 the residual background level.

207 $G(x)$ is defined in (2) where A is the amplitude of the
 208 Gaussian function, μ is the mean, and σ the standard deviation

$$209 \quad G(x) = Ae^{-\frac{(x-\mu)^2}{2\sigma^2}}. \quad (2)$$

210 $S(x)$ is defined as per (3) where B is the step function
 211 amplitude (expressed as a fraction of A) and $\text{erfc}(x)$ is the
 212 complementary error function, and the tail function, $T(x)$, is as
 213 per (4), where C is the tail function amplitude (expressed as
 214 a fraction of A) and m is the slope of the exponential

$$215 \quad S(x) = AB\text{erfc}\left(\frac{x-\mu}{\sigma\sqrt{2}}\right) \quad (3)$$

$$216 \quad T(x) = ACe^{\frac{x-\mu}{m\sigma}}\text{erfc}\left(\frac{x-\mu}{\sigma\sqrt{2}} + \frac{1}{m\sqrt{2}}\right). \quad (4)$$

217 The contribution due to the principal radionuclide over a
 218 complex continuum background of radiation is then calculated
 219 using (5), where N is then the number of counts corresponding
 220 to the photopeak, obtained by calculating the area under the
 221 Gaussian, $G(x)$

$$222 \quad N = \int_{\mu-n}^{\mu+n} G(x)dx \quad (5)$$

223 wherein n assumes a predetermined constant value indicative
 224 of a photon-energy interval sufficient to cover 3σ either side
 225 of the photopeak and the uncertainty in the N measurement
 226 is obtained by error propagation considering the obtained
 227 standard deviation in the fit variables (from the covariance
 228 matrix).

229 B. Modeling γ -Ray Log Depth Profiles

230 The response of a γ -ray logging tool can be represented as
 231 the total number of detected γ -ray counts due to the γ -emitting
 232 radioactive material present in the volume of investigation or in
 233 terms of the constituent proportions derived from analysis of a
 234 corresponding γ -ray spectrum. The contribution of individual
 235 isotopes can be evaluated and plotted as a function of depth
 236 from this analysis, yielding depth profiles for specific γ -ray
 237 lines.

238 Typically, a pulse function can be used to represent the
 239 variation in response intensity of the logging γ -ray tool as
 240 a function of depth in the vicinity of a radioactive anomaly in
 241 the ground. This can be interpreted in terms of the hypothetical
 242 response of a point detector at an infinitely slow logging speed
 243 (depth series) for a uniform zone of contamination. However,
 244 the boundaries of a pulse may not be defined sharply and
 245 pulses may have irregular shapes due to factors such as logging
 246 speed and measurement time, the size of the sensitive volume
 247 of the detector, variation of the spatial distribution of the
 248 source radioactivity in the bed formation, and changes in the
 249 volume of investigation from one measurement to another.

250 Logging tools are often used in boreholes in radioactive
 251 areas to locate contamination zones and to determine the
 252 distribution of migrating radioactivity from a source, as well
 253 as to identify and obtain relative proportions of specific
 254 nuclides within a given medium. These objectives can require
 255 careful analysis of the overall shape of the depth profile in
 256 specific regions where changes in intensity, corresponding to
 257 radioactive anomalies, are to be resolved to a sufficient degree.

258 Changes in shape of the intensity profile can be due to a
 259 combination of influences such as changes in activity, source
 260 dispersion, and the geometry of shielding materials. A source
 261 of radiation in a medium can be theorized as an extended
 262 homogeneous layer with a notional volume (extended depth
 263 vertically and horizontally relative to the orientation of the
 264 borehole) or as a point source (such as a ‘‘hot’’ particle)
 265 at a vertical/horizontal position to the borehole), as well as
 266 heterogeneous sources comprised of various point sources at
 267 different positions but within a defined volume [4]. In practice,
 268 the distribution of radioactivity in the ground is often complex
 269 and may comprise several configurations.

270 A scenario approximating to a point source in the ground,
 271 assessed with a single transit of logging system across a

range in depth spanning the position of the source, might yield a single peak shape that can be described by simple model with a small number of fitting parameters. A 1-D, PSF is an attractive option for the analysis of discrete photon depth spectra profiles of a point source near to a blind tube. However, such a function should encompass the entire activity profile, including an inner zone (corresponding to the core of the profile) and an outer zone with low numbers of counts present in its “wings.” While a Gaussian distribution might serve as a first approximation, the extremities of a profile can be more extensive than this is able to fit self-consistently. This introduces important uncertainties as to the depth at which a radioactive anomaly is discernible from the ambient.

An alternative to a Gaussian is the Moffat peak-like distribution because this accounts for the departure from Gaussian shape in the extremities on either side of the peak. A Moffat distribution is a Lorentzian continuous probability distribution modified with a variable power index. It is often described as a special case of the multivariate student- t distribution, specifically a distribution of a bivariate random variable (x, y) centered at zero (or as of the corresponding radius in this context). It has been used in astrophysics applications [13] to cater for seeing effects (see the following) in stellar profiles and for synapse image analysis concerning the nonuniform scattering of photons across the brain/cranial window of mammals [14].

In astronomy, “seeing” refers to image degradation of an astronomical object caused by atmospheric turbulence [13]. This results in brightness distributions (or radial intensity profiles) in captured, 2-D, ground-based images. Such abnormal radial intensities can manifest as irregular wings in the point-spread profiles that neither Gaussian nor Lorentzian distributions reproduce consistently, whereas a Moffat PSF can.

The standard, 2-D, Moffat PSF characterizes a spatial distribution of photons under the assumption of circular symmetry, i.e., a circular aperture, centered at the object centroid, as per g , where

$$g(x, y) = I \left[1 + \frac{(x - p_x)^2}{w_x^2} + \frac{(y - p_y)^2}{w_y^2} \right]^{-\beta} \quad (6)$$

where x and y in this context denote position, I is the amplitude, and p_x and p_y denote the centroid position of the profile in the image. The parameters w_x , w_y , and β account for the effect of photon scattering in a medium between the object and the detector recording the image, often referred to as seeing parameters that govern the width and the shape of a profile, respectively: w is a scale parameter that determines the width of the distribution and radius of a circle ($w = w_x = w_y$) in a 2-D image projection as per Fig. 1(a); β parameterizes the extent of the wings on either side of the peak of the distribution, correcting the anomalous slope for larger radii. Note that larger values of β result in a steeper slope and, when $\beta \rightarrow \infty$, the function tends to a Gaussian. Radii in one axis projection can be calculated from the full-width-at-half-maximum as equal to $(\text{FWHM}/2) = 2w(2^{1/\beta} - 1)^{1/2}$ or the full-width-at-tenth-maximum as equal to $(\text{FWTM}/2) = 2w(10^{1/\beta} - 1)^{1/2}$, based on the chosen percentage of the amplitude signal (desired level of significance). The parameter β influences the resulting radius.

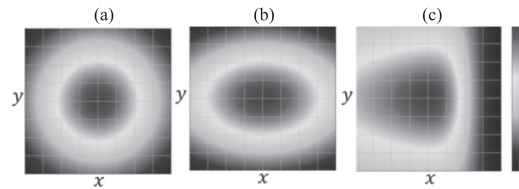


Fig. 1. Computer-generated images with color schemes representing the varying intensity levels across (x, y) coordinates for (a) symmetrical, (b) elliptical, and (c) asymmetric 2-D Moffat PSFs.

Population studies of dense stellar fields have proposed the use of modified 2-D Moffat PSFs because the spatial brightness of these distributions exhibits a degree of asymmetry. Analytically, this arises because, for elliptical dispersion, the parameter width is no longer equal for x - and y -projections (and thus $w_x \neq w_y$), as per Fig. 1(b), where the semi-major and the semiminor axes (w_x, w_y) are referenced to the central coordinates of the corresponding ellipse (x_0, y_0) . The FWHM varies symmetrically for each axis projection and at any specific inclination angle with the x -axis [15]. Asymmetry in a single-axis projection can be introduced via a position-dependent function in the corresponding width parameter w_x given by a sigmoid-type function $s(x) = 2w_x/(1 + e^{\gamma(x-x_0)})$ for x -axis asymmetry (on the y -axis, the profile is symmetrical). This asymmetric, 2-D, Moffat PSF represents a complex nonelliptical object [16] [see Fig. 1(c)] where $w_x \neq w_y$, and γ regulates the skewness of the peak profile.

Considering the photon dispersion depth profile of a vertical, 1-D scan of the simplest, point radioactive source distribution, a 1-D PSF is sufficient. Any eccentricity in the wings (corresponding to a contaminated zone boundary) is characterized by a Moffat PSF; any asymmetry is accounted for via an additional factor to yield a revised expression for g as per

$$g(x) = I \left[1 + \frac{(x - p_x)^2}{\left(\frac{2w_x}{1 + e^{\gamma(x-p_x)}} \right)^2} \right]^{-\beta} \quad (7)$$

where γ can be positive or negative, to indicate skew to the lower and higher values of a depth maximum, respectively, and null if symmetric, with β and w_x defined as positive. Higher values of β indicate a higher slope of the distribution wings, and higher values of w_x indicate a wider distribution. Note that the calculation of FWHM is more complex in non-symmetric cases, as an explicit isolated solution for $(x - p_x)$, and the determination of the radius (in a x -axis projection) requires the application of numerical methods, such as the Newton-Raphson method [17]. However, in instances where the fit yields a very small γ value, the previous FWHM expression can be employed for a quick assessment of the spread. This simplified scenario is used to define baseline values for γ , β , and w_x . Any detraction from these baseline values might suggest an extended or multicomponent source of radioactivity or discrepancies due to photon scatter arising due to density or structural changes of the ground surrounding a given borehole.

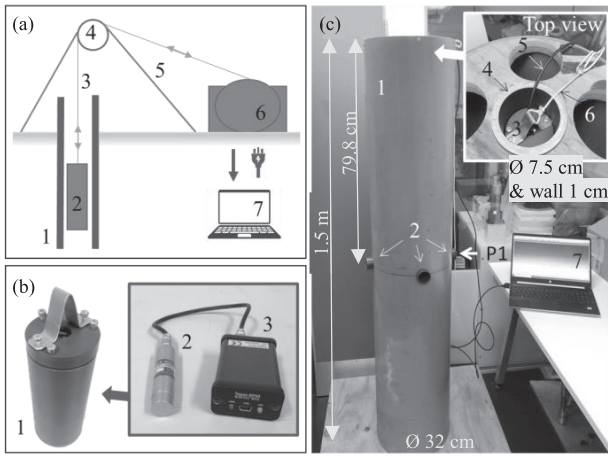


Fig. 2. (a) Schematic of the approach showing the borehole (1), the probe (2), tether (3), the pulley unit of the deployment system (4 and 5), and the winch (6) and laptop (7). (b) ABACUS probe unit (size $\text{Ø}7 \times 20$ cm) (1) including the detector (size $\text{Ø}1.5 \times 6.5$ cm) (2) and MCA (size $7 \times 4.5 \times 2.6$ cm) (3). (c) Laboratory setup including the testbed (1), the source ports (2), and the top view of the unit.

IV. MATERIALS AND METHODS

A. Blind-Tube Logging Probe Prototype

The blind-tube logging probe (BLP) used in this work, “ABACUS,” as per Fig. 2, comprises a γ -ray spectrometer and a digital multichannel analyzer (MCA) in an outer, cylindrical case. The spectrometer is made up of an inorganic scintillation detector and a silicon photomultiplier (SiPM) in a cylindrical, compact (physical size of $\text{Ø}1.5 \times 6.5$ cm²) hermetic unit (VS-1402-20, commercialized by Scionix, Netherlands). The scintillator is a $\text{Ø}9.5 \times 10$ mm² CeBr₃ crystal, and the crystal readout is a 6×6 mm² PM6660-SiPM (Ketek GmbH, Germany). The SiPM output is conditioned by a built-in preamplifier to cater for the effect of temperature; the influence of temperature on its light output was not catered for recognizing that the measurements were performed in a laboratory with some temperature compensation. Cerium bromide provides competitive γ -ray detection efficiency (with an effective atomic number, Z_{eff} , of 46, and a density of the material, ρ , of 5.2 g/cm³), energy resolution (3.2%–4% at 662 keV), high-count-rate capability (decay time = 17 ns), and radiation hardness ($<10^5$ Gy) [18].

The MCA used in ABACUS is a Topaz-SiPM supplied in a rugged and pocket-size (physical size of $7 \times 4.5 \times 2.6$ cm³) aluminum box with input and output connectors (commercialized by BrightSpec NV). It is among the smallest, full-featured MCAs currently available and performs pulse-height analysis of the signal from the scintillation detectors to provide energy spectra. It operates on a 5-V low-ripple, low-noise supply for the detector and can be interfaced to a laptop or notebook easily via USB 2.0 communication interface for power supply and data transfer. The unit includes a spectroscopy software interface. Note that by installing the MCA unit in the probe case, the detector output signal is digitalized before being sent to the surface, enabling signal transmission with less noise, distortion, and environmental interference [9].

The probe case has a simple cylindrical geometry and physical dimensions compatible with the dimensions of existing blind tubes. The γ -ray spectrometer is fixed parallel to

the central axis of the case and centered at the bottom. A collimator is not used, and hence, the detection response is assumed isotropic apart from the top side of the crystal where the electronics is housed. The signal processing module is placed on top of the detector and connected to it via a LEMO¹ connector. The case is made of plastic ($\text{Ø}70 \times 211$ mm long) with a top lid with a hole for the USB cable and a hook to aid deployment and recovery when in use.

B. Deployment System

A typical deployment system for the ABACUS probe comprises a winch by which the tool is lowered and retrieved, a sheave to add the change of the direction of the cable between the winch and the hole, and a high-resolution encoder for depth measurement. Typical logging cables (multicore wired) provide a combined means of data transfer, power supply, and mechanical support. Surface instruments, comprising a data logger or control unit, store the data and are used to control the winch system, to set the position of the probe within a borehole.

In the context of this work, a simplified deployment system has been used for laboratory-based tests in which a sheave and encoder are not used, with the probe lowered/raised manually with depth position measured using a hand-held, laser-based distance meter at the top of the blind tube. The logging cable then consists of two separate cables: a rope to support the weight of the probe and a 3-m-long USB cable for data transmission and power supply.

C. Blind-Tube Testbed

The blind-tube testbed used in this research is a laboratory-controlled monitoring well designed for radiation detection and photon depth-profile testing. It has been designed to calibrate the BLP response for a variety of scenarios (e.g., simple-to-complex spatial distributions of source and media) before conducting field measurements.

The testbed comprises an inner, vertical pipe at the center of an outer pipe fixed in a base, with four smaller tubes intersecting both pipes horizontally, fixed 80 cm from the top. The inner pipe represents the blind tube in this arrangement with the material and size of this pipe selected to replicate legacy blind tubes at nuclear sites, i.e., Sellafield, as close as possible; in this case, blind tubes lined with carbon steel with inner diameters ranging from 75 to 80 mm and wall thicknesses ranging from 6 to 10 mm. The carbon steel tube (European Tubes Ltd., U.K.) is 1.5 m long with an inner diameter of 75 mm and a wall thickness of 9.5 mm. The outer pipe functions as a material retainer or tank. It is 1.5 m long, 320 mm in diameter, made of plastic, and designed so that the space between the blind tube and the plastic outer pipe can be filled with material (such as sand) to recreate a vertical ground core, translating to about 113 mm of material surrounding the blind tube (not done in this work). The horizontal tubes create a void in the matrix material to enable sealed radioactive sources to be inserted and removed quickly and easily.

In this research, a scenario has been assumed comprising a single point source with the least degree of scattering possible

¹Registered trademark.

464 between source and detector, with the test pit left empty of
 465 material and a sealed source fixed close to the wall of the
 466 blind tube.

467 D. Experimental Method

468 A cesium-137 source with an activity of 304 kBq was
 469 inserted into the horizontal tube at position P1 (see Fig. 2). The
 470 BLP prototype was then lowered into the blind-tube testbed
 471 (described above) and fixed at various depth positions using
 472 a rope attached to the top of the testbed. The position of the
 473 probe in the pipe, d , relative to the top of the testbed, was
 474 determined using a hand-held laser position meter. The meter
 475 was placed on top of the tank, with its laser output directed
 476 downward toward the top surface of the logging probe.

477 These data were then converted into distance, D , between
 478 the top of the pipe and the center of the sensor element
 479 by considering the internal dimensions of the probe. Each
 480 spectrum was acquired for 1 h to achieve sufficient statistical
 481 precision for peak evaluation. The data were transferred via
 482 USB 2.0 to a laptop running the γ -ray spectroscopy software,
 483 and each spectrum was saved in the text file format. The
 484 following sections describe an algorithm written in python²
 485 used to analyze each obtained spectrum for a variety of depth
 486 positions.

487 E. γ -Ray Spectral Log Analysis

488 The analysis was divided into two stages. The photopeak
 489 model (1) is used first to characterize the γ -ray spectra
 490 recorded by the BLP. Each spectrum is the energy distribution
 491 of the photons (γ rays and X-rays) determined at a specific
 492 depth within the blind-tube testbed as per Fig. 3. Second, the
 493 depth profile fit is performed as per Fig. 4.

494 The photopeak model has been applied to each spectrum for
 495 each depth position, i , where increasing values of i correspond
 496 to increasing depth into the ground or, in this case, the testbed.
 497 An ROI defined between a lower L and upper U energy
 498 bounds is selected to initialize the method encompassing a
 499 peak, i.e., the 662-keV line of cesium-137. Initial U and L
 500 values were derived from a typical spectrum: L to the right of
 501 the Compton edge and U to the right of the photopeak where
 502 the count level approaches the level of background noise.

503 Least-squares minimization was used to optimize the fit
 504 of f [see (1)] to the data within the ROI at each depth i . The
 505 fitting algorithm starts with an initial fitting iteration to obtain
 506 initial values for the fit parameters (derived from a typical
 507 spectrum) and this is then optimized to obtain the parameters
 508 and their associated uncertainties. These values are saved, and
 509 the process is repeated for the next position. The method
 510 checks for errors in the fitting process (such as a failure of
 511 the fit or to find optimal parameters), adjusts where necessary,
 512 and repeats the process.

513 The ROI may be adjusted by reducing U by one channel to a
 514 lower energy until it equals μ (the centroid of the Gaussian).
 515 If the process still fails to fit the data, an error message is
 516 registered (since effectively no photopeak is detected) and the
 517 method moves on to the next position. Following the fitting

²Trademarked.

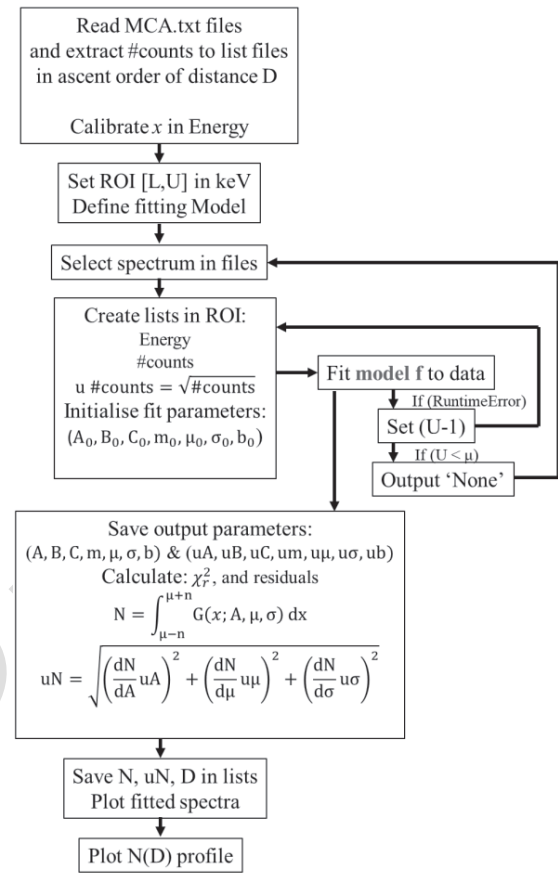


Fig. 3. Flowchart of the spectrum fitting process including the data flow.

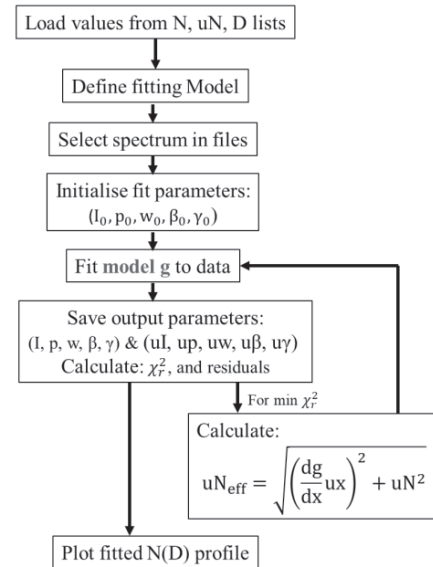


Fig. 4. Flowchart of the depth-profile fitting process.

518 process, (5) is used to calculate the total number of counts N_i 518
 519 corresponding to a number of counts under the photopeak, i.e., 519
 520 indicative of the level of cesium-137 662-keV γ rays detected 520
 521 at each position i . 521

522 The aim of the fitting process is to find values of 522
 523 unconstrained parameters based on a minimization using a 523
 524 Levenberg–Marquardt algorithm. In python, this is performed 524
 525 by the function `scipy.optimize.curve_fit()`; a chi-squared test of 525
 526 independence is used to assess the consistency of a given fit. 526

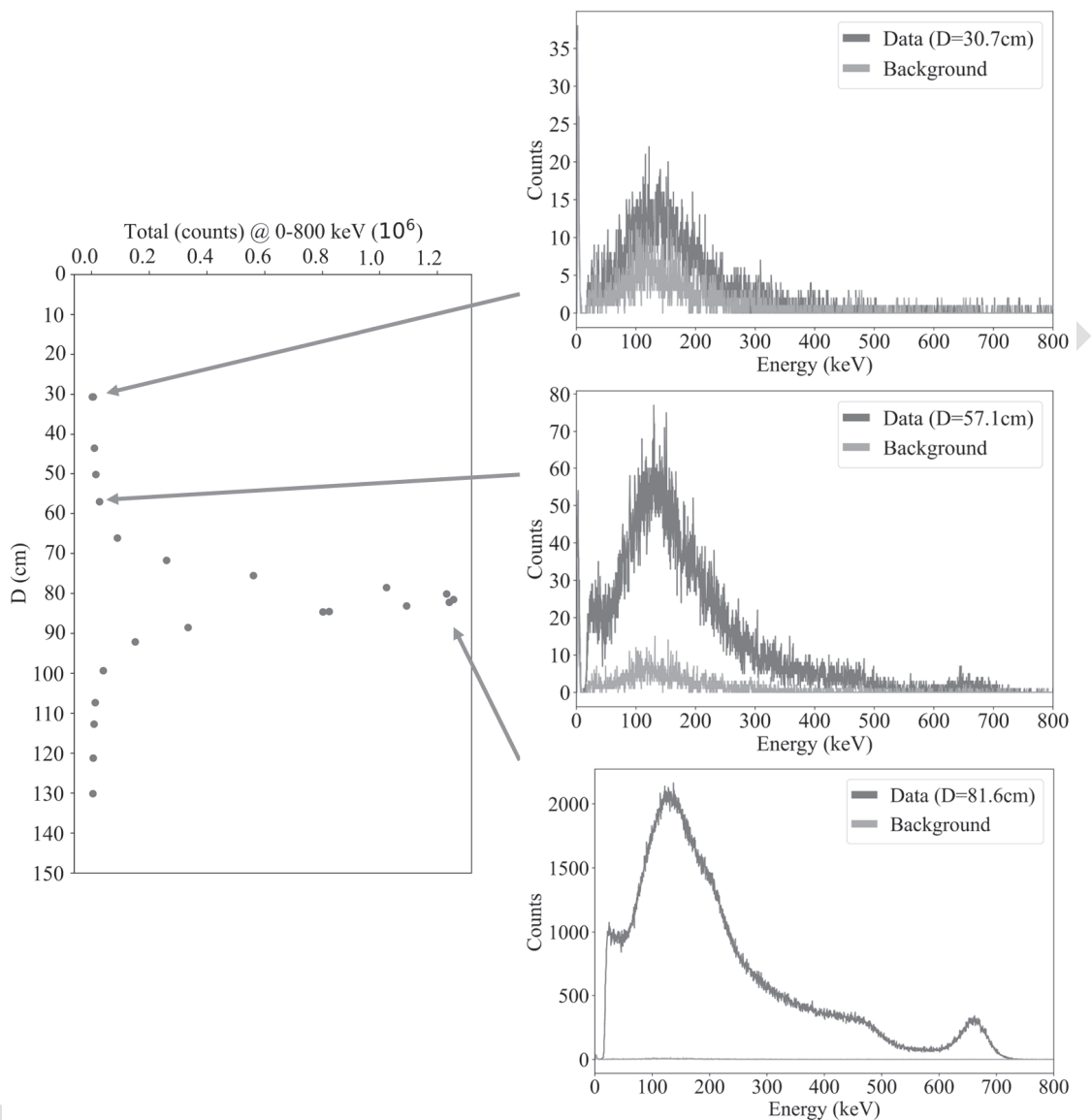


Fig. 5. Depth versus total counts for a single profile exercise (left) and example spectra for three different positions (right): 30.7, 57.1, and 81.6 cm.

V. RESULTS AND DISCUSSION

The γ -ray spectra obtained with cesium-137 at P1, and with the BLP prototype positioned at specific distances 30 up to 130 cm from the top pipe, are shown in Fig. 5. This illustrates that the intensity of the 662-keV peak is greater when the detector is close to the source and decreases when it is further away, as expected, with the highest intensity observed at the shortest possible source–detector separation. A wide scatter continuum is observed due to the effect of the surroundings and incomplete photon absorption in the detector crystal.

The sum of counts may be obtained by direct summation or by fitting an analytical function to the data. A Gaussian with an additional component to represent the low-energy tailing on the peak, f , was used, as per (1), with parameters as defined earlier. χ^2_v for the fits was ~ 1 , but the algorithm fails to fit peaks of small amplitude (< 15 counts). This error arises from the failure of the optimization algorithm to achieve convergence within the specified number of iterations and may be attributable to the model’s complexity and the presence

of noise on a low amplitude photopeak. Note that applying moderate smoothing techniques, such as the Savitzky–Golay filter [19], on spectra with low photopeak amplitudes prior to optimization process may address this issue and, consequently, enhance the accuracy of the profile encompassing the limits of the γ -ray depth profile (not done in this work). Fig. 6 shows an example of a fit for cesium-137. The number of counts under the peak N_p was extracted by integrating the Gaussian component of the optimized function (1), between 3σ on either side of the μ -peak value, plotted against the detector position in the blind-tube testbed, as per Fig. 6. These data describe an asymmetric PSF akin to astrophysical problems and have been fit with a Moffat function, g , with a skew component, as per (7), where the parameters are as defined earlier. Fig. 6 suggests an acceptable fit incorporating the asymmetric trend, which is superior when compared to Gaussian-type models (see Table I).

The amplitude term, I , can be used to estimate the activity or concentration of cesium-137 in the sample, provided that

527

528

529

530

531

532

533

534

535

536

537

538

539

540

541

542

543

544

545

546

547

548

549

550

551

552

553

554

555

556

557

558

559

560

561

562

563

564

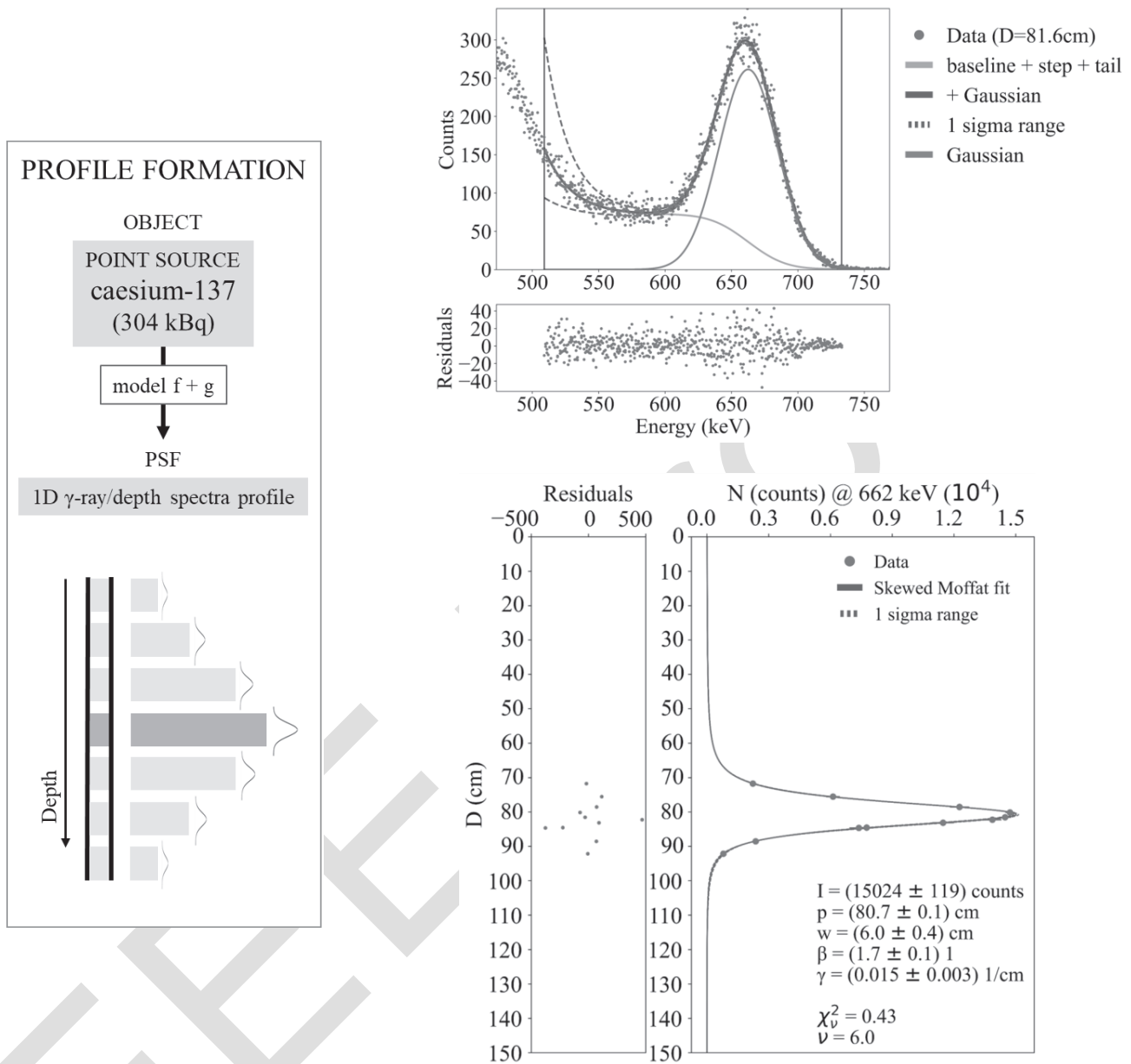


Fig. 6. Schematic of the depth profiling process (left) with an example spectrum (right, top) including the combination of fits comprising (1) and the depth profile obtained from an experimental scan (right, bottom) with the modified Moffat PSF fit as per (7), with the corresponding fit parameters: I represents the amplitude, p is the peak depth position, w refers to the width, β refers to the shape, and γ refers to the skewness term of the profile. The reduced chi-squared, χ^2_{ν} , was 0.43, with the number of degrees of freedom (ν) of 6.

TABLE I
PSF MODELS AND FIT PARAMETERS

Parameter	Gaussian	Skewed Gaussian	1-D Moffat	1-D Skew Moffat
A / counts	14493 ± 397	11806 ± 1569	14924 ± 209	15024 ± 119
μ / cm	80.5 ± 0.3	78 ± 1	80.5 ± 0.1	80.7 ± 0.1
σ / cm	4.3 ± 0.2	5.3 ± 0.7	7.1 ± 0.8	6.0 ± 0.4
β	-	-	2.2 ± 0.3	1.7 ± 0.1
γ / cm^{-1}	-	1.0 ± 0.5	-	0.015 ± 0.003
χ^2_{ν}	12.8	12.5	1.7	0.4
df	8	7	7	6

565 calibration is performed. The maximum peak height observed
 566 in this work was (15024 ± 119) cph (~ 4 cps) for a ^{137}Cs
 567 point source of activity of 304 kBq.

The position of the source is inferred from the fit in
 Fig. 6 associated with the centroid parameter, p , to give
 (80.7 ± 0.1) cm. P1 was positioned at (79.8 ± 0.5) cm,

568

569

570

highlighting a consistent result within the uncertainties (relative error $\sim 1\%$).

The width term, w , can be used to estimate the vertical spatial resolution of the system defined at 50% of the signal and given approximately by $2w_x(2^{1/\beta} - 1)^{1/2}$, i.e., (8.5 ± 0.6) cm.

The shape terms β and γ determine the rate of change of the width of the distribution (spread of radiation) in relation to the peak position p along the x -axis. These suggest a relative degree of attenuation that photons experience before reaching the sensor, influenced by factors such as shielding or the density of the surrounding media. Since, in this study, the setup was designed to minimize attenuation, the values obtained correspond to this scenario, as per (1.7 ± 0.1) and (0.015 ± 0.003) cm^{-1} for β and γ , respectively, and are intrinsic to this blind-tube testbed and detector system arrangement. Moreover, the γ value obtained is positive, very small but nonzero, indicating a slight asymmetry in the distribution (steeper on the right side of the peak centroid than the left). This effect may be due to an asymmetric attenuation, i.e., the presence of sensor case, electronics, and the length of the probe case where the MCA is positioned, on the back of the sensor crystal.

By analyzing the parameters (I , p , w , and β) and their corresponding three-standard deviations in both nonskewed and skewed Moffat models (Table I), the results indicate that all the corresponding parameters are similar within the 99.7% confidence range. This implies that the models yield similar fits to the data distribution, which is reasonable given that the obtained γ value is close to zero.

VI. CONCLUSION

In situ borehole monitoring of radioactivity is an important modality by which both the location and the composition of radioactive contamination entrained in groundwater and geological strata can be probed. However, photon spectra arising from this approach can be complex and varied, and hence, reliable analytical methods are necessary by which individual contributions to them can be estimated. Likewise, the point-spread distribution of photon count data that can arise with depth concerning a particular anomaly can be asymmetric due to inhomogeneities in the borehole surroundings and the influence of the monitoring instrumentation on scatter while in use underground.

In this research, the design and development of a prototype borehole monitoring probe and bespoke testbed have been described. The use of these is demonstrated in which the semiempirical model developed by Phillips and Marlow [9] has been combined with development of the Moffat PSF [13] to extract spectroscopic features and localization information, respectively. This approach, combined with the ABACUS BLP, yields a consistent indication of the depth of radioactive source positioned in a bespoke, blind-tube testbed. In future, these approaches will be targeted toward understanding more complicated source distribution scenarios, the proportion and spatial distribution of ^{137}Cs and ^{90}Sr in aqueous media, and progressing to active testing in the field.

ACKNOWLEDGMENT

The authors acknowledge useful discussions with B. Greenhalgh and T. Calverley.

REFERENCES

- [1] P. Hallington, J. Heneghan, and J. Graham. (2021). *RemPlex Summit Case Studies: Optimization of Remediation Planning Approaches Based on Lessons Learned at the Sellafield Site, U.K.* Accessed: May 4, 2022. [Online]. Available: <https://www.pnnl.gov/projects/remplex/case-studies#CaseStudy4>
- [2] J. Homilius and S. Lorch, "On the theory of gamma ray scattering in boreholes," *Geophys. Prospecting*, vol. 6, no. 4, pp. 342–364, 1958.
- [3] H. L. Nguyen et al., "Analysis of the relationship binding in situ gamma count rates and soil sample activities: Implication on radionuclide inventory and uncertainty estimates due to spatial variability," *J. Environ. Radioactivity*, vol. 192, pp. 349–361, Dec. 2018.
- [4] R. D. Wilson, C. J. Koizumi, J. E. Meisner, and D. C. Stromswold, "Spectral shape analysis for contaminant logging at the Hanford site," *IEEE Trans. Nucl. Sci.*, vol. 45, no. 3, pp. 997–1001, Jun. 1998.
- [5] J. R. Giles and K. J. Dooley, "High resolution gamma-spectroscopy well logging system," *J. Radioanal. Nucl. Chem.*, vol. 233, nos. 1–2, pp. 125b–130, Jul. 1998.
- [6] C. J. Koizumi, J. R. Brodeur, R. K. Price, J. E. Meisner and D. C. Stromswold, "High-resolution gamma-ray spectrometry logging for contamination assessment," *Nucl. Geophys.*, vol. 8, no. 2, pp. 149–164, 1994.
- [7] L. L. Gadeken, W. P. Madigan, and H. D. Smith Jr., "Radial distributions of ^{60}Co contaminants surrounding wellbores at the Hanford site," in *Proc. IEEE Nucl. Sci. Symp.*, vol. 1, 1995, pp. 214–218.
- [8] S. Elísio and M. J. Joyce, "Method and apparatus for determining attributes of a source of radiation," U.S. Patent P 347 121GB/CAB, Sep. 29, 2022.
- [9] G. W. Phillips and K. W. Marlow, "Automatic analysis of gamma-ray spectra from germanium detectors," *Nucl. Instrum. Methods*, vol. 137, no. 3, pp. 525–536, Sep. 1976.
- [10] J. Uher, G. Roach, and J. Tickner, "Peak fitting and identification software library for high resolution gamma-ray spectra," *Nucl. Instrum. Methods Phys. Res. A, Accel. Spectrom. Detect. Assoc. Equip.*, vol. 619, nos. 1–3, pp. 457–459, Jul. 2010.
- [11] P. Mortreau and R. Berndt, "Characterisation of cadmium zinc telluride detector spectra—Application to the analysis of spent fuel spectra," *Nucl. Instrum. Methods Phys. Res. A, Accel. Spectrom. Detect. Assoc. Equip.*, vol. 458, nos. 1–2, pp. 183–188, Feb. 2001.
- [12] A. Varley, A. Tyler, L. Smith, and P. Dale, "Development of a neural network approach to characterise ^{226}Ra contamination at legacy sites using gamma-ray spectra taken from boreholes," *J. Environ. Radioactivity*, vol. 140, pp. 130–140, Feb. 2015.
- [13] A. F. J. Moffat, "A theoretical investigation of focal stellar images in the photographic emulsion and application to photographic photometry," *Astron. Astrophys.*, vol. 3, p. 455, Dec. 1969.
- [14] T. M. Ryan, A. J. Hinojosa, R. Vroman, C. Papisavvas, and L. Lagnado, "Correction of z-motion artefacts to allow population imaging of synaptic activity in behaving mice," *J. Physiol.*, vol. 598, no. 10, pp. 1809–1827, May 2020.
- [15] G. Fiorentino et al., "On the use of asymmetric PSF on NIR images of crowded stellar fields," *Proc. SPIE*, vol. 9148, pp. 1301–1314, Aug. 2014.
- [16] S. K. Jensen Jr., S. D. Brittain, J. R. Najita, and J. S. Carr, "Modeling of CO rovibrational line emission of HD 141569," *Publications Astronomical Soc. Pacific*, vol. 133, no. 1028, Oct. 2021, Art. no. 104402.
- [17] J. P. Dedieu, "Newton-Raphson method," in *Encyclopedia of Applied and Computational Mathematics*, B. Engquist, Ed. Berlin, Germany: Springer, 2015.
- [18] S. Elísio, M. J. Joyce, J. Graham, and B. Greenhalgh, "An advanced blind-tube monitoring instrument to improve characterization of sub-surface radioactive plumes," in *Proc. EPJ Web Conf.*, vol. 253, 2021, p. 08005.
- [19] A. Savitzky and M. J. E. Golay, "Smoothing and differentiation of data by simplified least squares procedures," *Anal. Chem.*, vol. 36, no. 8, pp. 1627–1639, Jul. 1964.

625
626
627
628
629
630
631
632
633
634
635
636
637
638
639
640
641
642
643
644
645
646
647
648
649
650
651
652
653
654
655
656
657
658
659
660
661
662
663
664
665
666
667
668
669
670
671
672
673
674
675
676
677
678
679
680
681
682
683
684
685
686
687
688
689
690
691
692
693

AQ:6